

The Formation and Structure of a Strongly Magnetized Corona above Weakly Magnetized Accretion Disks

Kristen A. Miller and James M. Stone¹

Department of Astronomy, University of Maryland, College Park, Maryland 20742-2421

Received _____; accepted _____

¹also Institute of Astronomy, University of Cambridge, Madingley Road, Cambridge CB3 0HA, UK

ABSTRACT

We use three-dimensional magnetohydrodynamical (MHD) simulations to study the formation of a corona above an initially weakly magnetized, isothermal accretion disk. The simulations are local in the plane of the disk, but extend up to 5 vertical scaleheights above and below it. We describe a modification to time-explicit numerical algorithms for MHD which enables us to evolve such highly stratified disks for many orbital times. We find that for initially toroidal fields, or poloidal fields with a vanishing mean, MHD turbulence driven by the magnetorotational instability (MRI) produces strong amplification of weak fields within two scale heights of the disk midplane in a few orbital times. Although the primary saturation mechanism of the MRI is local dissipation, about 25% of the magnetic energy generated by the MRI within two scale heights escapes due to buoyancy, producing a strongly magnetized corona above the disk. Most of the buoyantly rising magnetic energy is dissipated between 3 and 5 scale heights, suggesting the corona will also be hot. Strong shocks with Mach numbers $\gtrsim 2$ are continuously produced in the corona in response to mass motions deeper in the disk. Only a very weak mass outflow is produced through the outer boundary at 5 scale heights, although this is probably a reflection of our use of the local approximation in the plane of the disk. On long timescales the average vertical disk structure consists of a weakly magnetized ($\beta \sim 50$) turbulent core below two scale heights, and a strongly magnetized ($\beta \lesssim 10^{-1}$) corona which is stable to the MRI above. The largescale field structure in both the disk and the coronal regions is predominately toroidal. Equating the volume averaged heating rate to optically thin cooling curves, we estimate the temperature in the corona will be of order 10^4 K for protostellar disks, and 10^8 K for disks around neutron stars. The functional form of the stress with vertical height is best described as flat within $\pm 2H_z$, but proportional to the density above $\pm 2H_z$.

For initially weak uniform vertical fields, we find the exponential growth of magnetic field via axisymmetric vertical modes of the MRI produces strongly buoyant sheets of magnetic energy which break the disk apart into horizontal channels. These channels rise several scale heights vertically before the onset of the Parker instability distorts the sheets and allows matter to flow back towards the midplane and reform a disk. Thereafter the entire disk is magnetically dominated and not well modeled by the local approximation. We suggest this evolution may be relevant to the dynamical processes which disrupt the inner regions of a disk when it interacts with a strongly magnetized central object.

Subject headings: accretion disks – instabilities – MHD – turbulence

1. Introduction

The observed spectrum of thin accretion disks in many systems suggests that the diffuse upper layers are heated to much higher temperatures than the midplane, i.e. that such disks have coronae. For example, disks around compact objects (Nandra & Pounds 1994), CVs (Yi & Kenyon 1997), classical T Tauri stars (CTTS, Kwan 1997), and Herbig AeBe stars (Najita et. al. 1996) all show evidence for the existence of a corona.

One simple explanation for the presence of a corona above a thin disk is that it is produced by external irradiation from the central object (or the central, hotter regions of the disk itself). A variety of authors have investigated the vertical structure of a thin disk atmosphere using radiative transfer calculations (Wade & Hubeny 1998; Dove et. al. 1997; Haardt & Maraschi 1991) including the effect of irradiation from the central regions (D'Alessio et. al. 1998; Wood et. al. 1996). Such studies often find the diffuse upper layers of the disk are much hotter than the midplane. However, it should be noted that including a sophisticated treatment of the internal dynamics of the disk into such calculations is a formidable task, thus important ingredients such as the vertical profile of the heating rate due to accretion usually must be assumed using, e.g., the “ α -disk” prescription (Shakura & Sunyaev 1973).

A second possible explanation for coronae above accretion disks is that they are a direct consequence of the internal dynamics of the disk itself rather than a radiative transfer effect, much in the same way the solar corona is thought to be heated by dynamical processes lower in the atmosphere. This possibility was first suggested as a mechanism to explain the X-ray emission of Cygnus X-1 (Liang & Price 1977, Galeev et. al. 1979) and of Seyfert AGN (Liang & Thompson 1979). In a detailed investigation by Stella & Rosner (1984), “magnetic buoyancy-driven” convection of strong flux tubes produced by shear in the disk was identified as the most promising source of the vertical energy flux needed to heat a corona. Although it was recognized that shear amplification of the field would result in stresses on the fluid that might give rise to angular momentum transport in the disk (Coroniti 1981; Sakimoto & Coroniti 1981), and that buoyancy might be the primary saturation mechanism for the field (Sakimoto & Coroniti 1989), modeling the coupled amplification, saturation, and angular momentum transport processes from first principles required multidimensional MHD models that were beyond the scope of these pioneering studies. Nonetheless, these early models were able to fit observations well enough to suggest that the internal dynamics of the disk might play an important role in determining the vertical structure.

Strong magnetic fields (which have $\beta \leq 1$, where $\beta \equiv 8\pi P/B^2$ with P the thermal pressure, and B the magnetic field strength) in a stratified accretion disk atmosphere are subject to both the Parker and magnetic interchange instabilities (e.g. Stella & Rosner 1984). As an extension of the earlier work discussed above, the nonlinear evolution of these instabilities has been the subject of recent sophisticated numerical MHD modeling (Kamaya et. al. 1997; Basu et. al. 1997; Chou et. al. 1997; Matsumoto et. al. 1993; Kaisig et. al. 1990). Although such studies have helped clarify the effect of magnetic buoyancy in determining the vertical structure of the disk, they do not address the field amplification process itself, and therefore cannot investigate questions such as how strong flux tubes are formed in the disk in the first place. It is clear that field amplification, buoyancy, and angular momentum transport processes are all highly coupled, and therefore must be studied in concert for a complete picture.

In recent years, our understanding of angular momentum transport processes in accretion disks has progressed rapidly, in part due to the identification of the magnetorotational instability (MRI) in weakly magnetized accretion disks, and the realization of the fundamental role it plays in the process (see the review of Balbus & Hawley 1998 for a complete discussion). Time-dependent MHD simulations have demonstrated that the MRI saturates as MHD turbulence in three-dimensions (Hawley, Gammie, & Balbus 1995a, hereafter HGB1), and that this turbulence drives a non-helical dynamo which produces strong amplification of the magnetic field (Hawley, Gammie, & Balbus 1995b, hereafter HGB2; Brandenburg et al. 1995, hereafter BNST; Stone et al. 1996, hereafter SHGB; Brandenburg 1998). Knowledge of the field amplification process allows us to address the problem of the formation of a disk corona from first principles. Tout & Pringle (1992) have presented an interesting analytic argument for the formation of a heated disk corona via a cyclic process involving the MRI, the Parker instability, and reconnection. However, the full details of such a (nonlinear) cycle require computational studies of the nonlinear evolution of the MRI in stratified disks. Current studies show that while buoyancy does result in a significant vertical flux of magnetic energy, it is not the dominant saturation mechanism for the instability: instead local dissipative processes dominate (BNST, SHGB). Still, these results hint at the possibility of the formation of a disk corona via buoyant rise of dynamo amplified magnetic field in that the scale height of the field was much larger than that of the gas, leading to a rapid decrease of β with height.

To date numerical simulations of the MRI in stratified disks have been limited by the relatively small vertical extent that can be included in the calculations. This limit is imposed by the enormous range in dynamical timescales in a stratified disk: the density falls so rapidly with height in an isothermal disk ($\rho \propto \exp(-z^2)$) that the Alfvén speed becomes very large in the upper layers. For a time-explicit numerical algorithm (in which the timestep is limited in part by the crossing time of an Alfvén wave across a grid zone), this makes calculations for many orbits of the disk impracticable with current computer resources. Thus, the simulations of BNST and SHGB were limited to two scale heights above the disk midplane, which was not enough to see the transition from a weakly magnetized turbulent core to a strongly magnetized corona which was stable to the MRI. Moreover, it is not clear what the effect of the boundary conditions applied at two scale heights may have on the field strength and geometry in this region. Ideally, one would like to apply outflow boundary conditions that allow mass, energy, and momentum to leave the computational domain, however, as discussed in SHGB, it is not possible to prescribe a self-consistent outflow boundary condition for a highly tangled, strong magnetic field without exerting anomalous stresses on the fluid near the boundary. Thus, in most of the simulations described by SHGB, periodic boundary conditions were applied at the vertical boundaries which, although they are clearly not a good representation of a real system, are not significantly less realistic than other viable choices, such as reflecting walls. A few simulations presented by SHGB which used different boundary conditions demonstrated that the vertical profile of horizontally averaged quantities near the midplane was not changed, indicating that the vertical structure is relatively independent of the boundary conditions. Moreover, the simulations of BNST used reflecting boundary conditions with a non-zero vertical component to the magnetic field (so that the turbulence in the disk generates a time-dependent current on the boundary); the resulting vertical structure of the disk was not significantly different than that reported by SHGB.

In this paper, we describe an extension to time-explicit MHD algorithms which removes the timestep constraint imposed by the divergence of the Alfvén speed in regions of very low density, and therefore allows numerical simulations over many orbital times of a disk

which spans many scale heights in the vertical extent. We use this extension to study the evolution of weakly magnetized, isothermal stratified disks over many orbital times using a grid which extends 5 scale heights above the disk midplane. We show that for a variety of initial field strengths and geometries, buoyantly rising magnetic field generated by MHD turbulence driven by the MRI near the midplane of the disk forms a strongly magnetized ($\beta \ll 1$) corona above two scale heights. Because it is strongly magnetized, the corona is stable to the MRI, and moreover the field becomes nearly force-free there (i.e. $(\nabla \times \mathbf{B}) \times \mathbf{B} \approx 0$). Thus, the field is no longer highly tangled near the upper boundary, and we are able to apply outflow boundary conditions appropriate to the system. These simulations allow us to investigate the formation and structure of a magnetized corona by calculating from first principles the coupled field amplification, buoyancy, and angular momentum transport processes. We are also able to measure properties such as the vertical profile of the stress and dissipation rate in the disk which may be useful in other contexts (such as detailed radiative transfer calculations of accretion disk atmospheres). Our models are still limited by the fact that they are local in the horizontal plane, which as we discuss may affect processes such as the generation of magnetocentrifugal winds from the disk surfaces. However, fully global models using the methods described here are underway.

The paper is organized as follows: in §2 we describe our numerical methods, in §3 we present the evolution of a variety of weak magnetic field configurations in stratified disks which span many vertical scale heights, in §4 we discuss the implications of our results for the vertical temperature profiles in CTTS and compact objects, and in §5 we conclude.

2. Numerical Methods

We solve the equations of compressible MHD including the effects of resistivity in the “shearing box” approximation (see HGB1 for a detailed description). That is, we adopt a frame of reference which is local, Cartesian, and corotates with the disk at angular frequency Ω corresponding to a fiducial radius R_o . In this local frame, we use spatial coordinates $x = (R - R_o)$, $y = (R\phi - \Omega t)$, and z . Assuming a Keplerian rotation profile and expanding within a small volume about the fiducial radius ($\Delta R \ll R_o$), the equations of motion can be expressed as:

$$\frac{\partial \rho}{\partial t} + \nabla \cdot \rho \mathbf{v} = 0, \quad (1)$$

$$\frac{\partial \mathbf{v}}{\partial t} + \mathbf{v} \cdot \nabla \mathbf{v} = -\nabla P/\rho + \frac{1}{\rho c} (\mathbf{J} \times \mathbf{B}) - 2\Omega \times \mathbf{v} + 3\Omega^2 x \hat{\mathbf{x}} - \Omega^2 z \hat{\mathbf{z}}, \quad (2)$$

$$\frac{\partial \mathbf{B}}{\partial t} = \nabla \times (\mathbf{v} \times \mathbf{B}) + \frac{c^2 \eta_0}{4\pi} \nabla^2 \mathbf{B}, \quad (3)$$

where \mathbf{J} is the current. The third and fourth terms on the RHS in the momentum equation [2] represent Coriolis and tidal forces in the rotating frame of reference, while gravitational acceleration in the vertical direction is represented by the last term. The final term in the induction equation [3] allows for field dissipation through an Ohmic resistivity with a constant magnitude η_0 . We assume isothermality and adopt an ideal gas equation of state with constant temperature, T , specified by our choice of the sound speed, c_s (see below). By adopting an isothermal equation of state we assume that all thermal energy generated through the dissipation of kinetic and magnetic energies is immediately and efficiently

radiated away and that there is an inflow of heat to adiabatically expanding regions (such as the buoyant magnetic flux tubes described in §3 below). Without a more sophisticated treatment of the thermodynamics of the gas, we cannot directly measure temperatures produced in our dynamical models (although by equating the energy dissipation rate measured in our simulations with an optically thin cooling rate, we can *estimate* equilibrium temperatures that might be reached in the corona, see §4). Moreover, if the vertical structure of the disk is significantly altered due to heating by the MRI, the rate of energy transport via buoyancy, and therefore the properties of the corona, may be affected. Also, we note that the assumption of isothermal evolution may increase the buoyancy of the flux tubes (see Torkelsson 1993) although this effect has not been studied in three dimensions. However, dynamical models which include a realistic treatment of radiation transport within an optically thick midplane and optically thin upper layers are beyond the current investigation.

We note that the current (the second term on the RHS in equation [2]) has been modified to include Maxwell’s displacement current (e.g. Jackson 1975); see the appendix for the definition of \mathbf{J} as it is used here. Physically, the displacement current limits the speed of propagation of electromagnetic waves to the constant c . With the usual assumptions of ideal MHD, it can be dropped from the system. We keep it here to limit the propagation velocity of Alfvén waves to a constant $c = c_{lim}$, where we set c_{lim} to be a value much less than the speed of light, but much larger than any relevant propagation speed within the disk. We further discuss the implications of including the displacement current in the evolution equations, and describe a technique for constructing a finite-difference approximation to the equation of motion [2] including it, in the appendix.

We use an initial equilibrium state consisting of a density distribution which is constant on horizontal planes and follows a Gaussian profile in the vertical coordinate,

$$\rho(x, y, z) = \rho_o e^{-z^2/H_z^2}, \quad (4)$$

where $H_z^2 = 2c_s^2/\Omega^2$ is the thermal scale height. Our disk is thin; i.e., $H_z/R = 0.01$. Initially all components of the velocity are zero except $v_y = \Omega x$. The choice of Ω is arbitrary in the shearing box formalism; for comparison with SHGB, we choose $\Omega = 10^{-3}$ and $2c_s^2 = 10^{-6}$ (which yields $H_z = 1$). Adopting $\rho_o = 1$, our initial pressure at the disk midplane is thus $P_o = 5 \times 10^{-7}$. To seed the MRI, random perturbations with amplitudes of order $0.001c_s$ are added to the velocities.

We study the evolution of three different initial magnetic field geometries: 1) a purely toroidal field, 2) a Zero Net Z (ZNZ) field, and 3) a uniform B_z field. The purely toroidal field is initialized only within $|z| \leq 2H_z$ such that $\beta = 25$ is constant within this region. The ZNZ field is generated by finite-differencing the following vector potential:

$$A_x = \begin{cases} \sqrt{2P_o/\beta(0)} \cos(2\pi x) \cos(y) & : |z| \leq 2H_z \\ \sqrt{2P_o/\beta(0)} \cos(2\pi x) \cos(y) e^{-(|z|-2H_z)^4} & : 2H_z < |z| < 4H_z \\ 0 & : |z| \geq 4H_z \end{cases} \quad (5)$$

where $\beta(0) = 25$ is the plasma parameter at the disk midplane. This vector potential generates a field which has only a vertical component $B_z \propto \sin(2\pi x) \cos y$ within two scale heights, and which is closed via loops between 2 and 4 scale heights. This configuration has

a null mean within $\pm 2 H_z$. Thus, within two scale heights, this geometry is equivalent to the ZNZ field studied extensively by SHGB. Finally, the uniform \hat{z} field is a constant field initialized over the whole grid, with $\beta(0) = 25$.

Our simulations are computed using the 3D version of the ZEUS code (Stone & Norman 1992a, 1992b). The Ohmic resistivity term is differenced using the method described in Fleming et. al. (1999). These authors found that $Re_M \equiv H_z c_s / \eta \leq 10^4$ ultimately quenches the MRI after many orbital times if the initial field configuration has a zero mean. In order to explicitly measure the reconnection and resistive heating rate in the corona, we have computed several models with $Re_M = 20,000$, which, for the numerical resolutions used here, is large enough to resolve the resistive lengths but small enough not to completely damp the turbulence driven by the MRI.

Our simulations consist of a grid of size $1H_z \times 10H_z \times 10H_z$, with a range of $-0.5H_z$ to $0.5H_z$ in the \hat{x} direction, 0 to $10H_z$ in the \hat{y} direction, and $-5H_z$ to $5H_z$ in the \hat{z} direction. We have also computed a model in which the horizontal extent of the box is increased by a factor of two. Our standard resolution is $32 \times 64 \times 128$ grid zones. We partition the zones in the vertical direction such that there are 64 zones in the region $|z| \leq 2H_z$; thus, inside this region our resolution is the same as SHGB. Above $|z| = 2$, the grid zones in the vertical direction increase logarithmically. We note that we have run one simulation with a grid which is nonuniform over the entire vertical domain to test that our choice of nonuniform zone spacing above $\pm 2H_z$ does not affect the results reported here (particularly that it does not affect the vertical structure described below). There were no qualitative differences between the test simulation and our fiducial model (some quantitative differences did develop within $\pm 2H_z$ due to differences in resolution). We have also run some higher resolution simulations to test the effect of resolution on our results. Such simulations are computationally intensive, prohibiting very high resolution runs.

In the \hat{x} and \hat{y} directions, we adopt the periodic shearing sheet boundary conditions described in HGB1. In the \hat{z} direction, we have implemented free (outflow) boundary conditions which allow mass, energy, momentum, and magnetic field to leave the grid. As described in Stone & Norman (1992a; 1992b), such outflow boundary conditions in the ZEUS code are implemented by using a constant (zero slope) projection of all the dynamical variables into the boundary zones.

3. Results

Table 1 lists the properties of the simulations discussed in this paper. Column 1 gives the identifier for each run; column 2 gives the value of β at the disk midplane; column 3 indicates the value of Re_M ; and column 4 gives the value of c_{lim} used in the displacement current. Columns 5 and 6 list our numerical resolution and the ratio of the critical wavelength, λ_c (calculated using equation 15 of HGB1), at the midplane to the grid size, which is given by Δy for the toroidal field runs and by Δz for the B_z runs. When this ratio is greater than 5, the fastest growing wavelengths are well resolved (see HGB1). Column 7 indicates the total time of the simulation in orbits. Columns 8, 9, and 10 give the time and space averaged values of the magnetic energy and the azimuthal (\hat{y}) components of the Maxwell and Reynolds stress for the regions $|z| \leq 2H_z$ (hereafter referred to as the “disk”) and $|z| > 2H_z$ (hereafter referred to as the “corona”); these quantities have all been

normalized to the initial pressure at the midplane. If we adopt the Shakura-Sunyaev α convention, the time averaged value of α for each simulation is simply the sum of columns 9 and 10.

3.1. Toroidal Field Simulations

We have performed toroidal field simulations with and without explicit resistivity (the runs with resistivity have been performed at two different resolutions); these are listed in Table 1 with the prefix “BY.” Our fiducial run (BY1) is a standard resolution, nonresistive run with $\beta = 25$ in the magnetized region ($|z| \leq 2H_z$). This simulation has been run for 50 orbital times. The critical wavelength for this run corresponds to $8.31\Delta y$; thus initially it is well resolved.

Figure 1 is a space-time plot showing the variation of horizontally averaged magnetic (top panel) and kinetic (bottom panel) energies as a function of vertical height and orbital time. The plot is constructed from the two dimensional function $F(z, t)$ by averaging each quantity f in the horizontal plane:

$$F(z, t) = \frac{\iint f(x, y, z, t) dx dy}{\iint dx dy}. \quad (6)$$

The plot of kinetic energy clearly shows the development of strong fluctuations associated with turbulence in the disk core after approximately 4-6 orbits driven by the nonlinear evolution of the MRI. We note that the growth rate and saturation time of the toroidal modes of the MRI observed here are in agreement with the toroidal field simulations of HGB1 (c.f. their figure 8) and SHGB (c.f. their figure 7). From the plot of the magnetic energy, periodic rise of buoyant magnetic field from the disk core over a few orbital times is clearly evident. The magnetic energy in buoyantly rising structures reaches a maximum at approximately $2.5 H_z$ and then decreases. Thus, buoyancy appears to add both magnetic flux and heat (through the dissipation of magnetic energy) into the region $z > 2.5H_z$. Since kinetic energy is dominated by the mass distribution, comparison of the spacetime plots of the kinetic and magnetic energies indicate that the buoyantly rising field carries a small amount of mass into the coronal region. Only a small fraction of the mass and magnetic energy escapes the grid through the vertical boundaries; most remains in the corona. At the end of the simulation, the value of β at the midplane yields a ratio of $\lambda_c/\Delta y = 6.14$; thus, the fastest growing wavelengths are still resolved.

To illustrate the vertical structure produced by the MRI, Figure 2 plots horizontally averaged values of the density, β , kinetic and magnetic energies, and the azimuthal components of the Maxwell and Reynolds stress averaged over orbits 25 through 50, after the saturation of the MRI. We also list in Table 2 the volume-averaged values of each component of the magnetic and kinetic energies, the off-diagonal components of the Maxwell stress, the azimuthal component of Reynolds stress, and the density in the disk and coronal regions averaged over the same times. The graph of density shows that it is still roughly Gaussian. Flaring occurs in the wings due to the transport of mass into the corona via buoyant flux (from Figure 1 the expelling of fluid from the disk into the coronal region is periodic and correlated with the rise of magnetic flux). However, the inner regions of the disk remain almost unchanged; the total mass in the corona is only 1.03 % of the total mass within $2H_z$. Table 2 confirms that the coronal densities are two orders of magnitude less

than in the disk midplane, and indicates that there are significant fluctuations in coronal region, with $\langle \delta\rho^2 \rangle^{1/2}/\langle \rho \rangle \approx 0.37$. The plasma β is greater than one inside the disk and increases to nearly fifty at the midplane, roughly twice its original value. This means that the core of the disk remains unstable to the MRI throughout the simulation. Above $\pm 2H_z$, β is $\lesssim 0.7$, confirming that a magnetically dominated corona has indeed been produced. Above $\pm 2.5H_z$, β becomes small enough that λ_c exceeds $10H_z$ (the domain size in the azimuthal direction); this is why this region is stable to the MRI. Overall, β varies by more than three orders of magnitude from the corona to the disk midplane. The magnetic and kinetic energy plots also show that the corona is magnetically dominated. The magnetic energy in the coronal region exceeds the kinetic by more than an order of magnitude. Note that the magnetic energy in the corona has increased from zero to $0.042 P_o$ due to the rise of flux from the disk. It is approximately constant within the disk core. The magnetic energy peaks at roughly $\pm 2H_z$; this same behavior was observed by SHGB (a further indication that the vertical magnetic energy profile described by these authors was not entirely a product of the periodic vertical boundary condition they used). The scale height of $B^2/(8\pi)$ is roughly twice the density scale height. Referring to Table 2, we see that the azimuthal component of magnetic energy strongly dominates in both the disk and coronal regions. The radial component of the kinetic energy is about a factor of two greater than the vertical and azimuthal components in the disk. In the corona, however, $\rho\delta v_y^2/2P_o$, which measures the energy in the velocity fluctuations, is nearly two orders of magnitude greater than the other components.

In order to ensure the vertical profiles and volume averaged values shown in Figure 2 and Table 2 respectively are not influenced by the time period over which they were averaged, we have reconstructed them with data which has been time-averaged over orbits 15 through 50 (note that this period includes the strong transient peak in magnetic energy associated with the initial growth of the toroidal field MRI evident around orbit 10 in Figure 1) and over orbits 35 through 50 (beginning the averages well after the time when this initial peak has faded). We find that the time averages which begin at orbit 15 (see columns 8,9, & 10 of Table 1) and those which begin at orbit 35 lead to nearly the same vertical profiles and volume-averaged values as reported in Figure 2 and Table 2, indicating these values are not dominated by transients associated with any particular period of evolution. Moreover, in §3.1.2, we show that higher resolution simulations produce similar profiles, and in §3.2 we show that other field geometries also lead to similar profiles. This suggests the vertical structure reported here for our fiducial model is a general outcome of the evolution of the MRI in highly-stratified disks.

From Figure 2, we see that the average of the azimuthal component of the Maxwell stress within $\pm 2 H_z$ is a factor of 4.05 greater than the azimuthal component of the Reynolds stress, consistent with the toroidal field simulations of SHGB. This indicates that the turbulence and angular momentum transport within the disk are magnetically dominated. The profile of the Reynolds stress component is dominated by the density (although it is slightly flatter within the disk region), while that of the Maxwell stress shows a very different pattern. Note that the azimuthal component of the Maxwell stress is fairly constant within the disk region, rising only slightly (less than a factor of 2) at the disk midplane and edges ($\pm 2H_z$). This means that α is fairly constant in the disk; our simulations yield an average value of 0.027 for the α parameter within the disk core. Again, we note that we find approximately the same value of α ($\lesssim 0.03$) whether or not we include the initial period when the MRI is saturating when we perform the temporal average. Thus, even though magnetic energy decreases slightly toward the end of the simulation (see figure 5), significant angular momentum transport continues to take place.

In the corona, we find that the azimuthal components of the Maxwell and Reynolds stresses drop sharply by 1-2 orders of magnitude over only $3 H_z$. The dramatic decrease in stress as we move into the coronal region indicates both that the transport rate has dropped and that the flow is much less turbulent here. The average value of the azimuthal component of the Maxwell stress in the coronal region is a factor of 5.0 smaller than in the disk (see Table 2), indicating the magnetic field is much less tangled. We find that the profile of the combined azimuthal stress as a function of vertical height is approximately flat within $\pm 2H_z$ and declines as e^{-z^2} above $\pm 2H_z$. Therefore, the azimuthal component of the combined stress does not follow the density profile within the disk core.

Figure 3 is a space-time plot of the off-diagonal components of the Maxwell stress tensor, as well as the azimuthal component of the Reynolds stress tensor. Note that all components except the $B_x B_z$ component of the Maxwell stress are largest in the region $|z| \leq 2H_z$, confirming that the disk flow is turbulent while the coronal flow is smoother. However, although the magnitudes of the stresses are much lower in the corona than in the disk, both regions are characterized by large fluctuations ($\langle (\delta f^2)^{1/2} \rangle / \langle f \rangle \approx 1.0$ (10.0 for the $B_x B_z$ and the $B_y B_z$ components) over the whole grid - see Table 2). The $B_x B_z$ component peaks between 2-3 H_z , just above the core of the disk, in the region where the magnetic energy begins to dissipate. B_z has a local maximum in this region as well, indicating that the field geometry is most strongly bent upwards by buoyancy between 2-3 H_z . The azimuthal component of the Reynolds stress confirms that the disk remains turbulent throughout the simulation. Diagonal streaks in the azimuthal components of the Maxwell and Reynolds stresses are clearly associated with the rising magnetic energy. Peaks in both (but particularly in the azimuthal component of the Maxwell stress) can be seen in the rising flux tubes. The $B_x B_z$ and $B_y B_z$ terms are two (one) orders of magnitude smaller than the azimuthal component of the Maxwell (Reynolds) stress (see Table 2) and show a highly sporadic pattern. This suggests that pressure is a more dominant force than the off diagonal components of the stress in leading to disk flaring. The $B_y B_z$ term is of particular interest as it is associated with the formation of a magnetocentrifugal wind. Our fiducial simulation produces an average value of $3.71 \times 10^{-4} P_o$ for $B_y B_z$ above $\pm 2H_z$, suggesting that only a very weak, unsteady wind is produced. We note, however, that the use of shearing sheet boundary conditions in the radial direction enforces a Keplerian rotation profile throughout the entire grid, even in the upper regions where the plasma is magnetically dominated. This may strongly affect the formation of a magnetorotational wind. Across the outer vertical boundary, average mass flux $\dot{M} = 2.21 \times 10^{-4} \sigma_d c_s$, where σ_d is the surface density at the disk “surface,” taken to be $\pm 2H_z$.

Above $\pm 2H_z$, the azimuthal components of both Maxwell and Reynolds stresses drop sharply, decreasing by more than an order of magnitude. The low value of the Reynolds term in the coronal region is, however, more a reflection of the low coronal densities than an indication of smooth, quiescent flow (c.f. Table 2 which indicates that $\rho \delta v_y^2 \sim 0.4 - 0.9 P_o$ in the corona). The coronal region is, in fact, in a highly dynamic state dominated by shocks. Figure 4 shows the vertical profile of the horizontally averaged rms velocity dispersion normalized by the sound speed, i.e.,

$$\left\langle \frac{(\Delta v)^2}{c_s^2} \right\rangle^{1/2} = \sqrt{\frac{\iint (\delta v_x)^2 + (\delta v_y)^2 + (\delta v_z)^2 dx dy}{c_s^2 \iint dx dy}}. \quad (7)$$

The profile shown in Figure 4 has been averaged over snapshots taken at seven equally spaced orbital times, between orbits 25 and 50. The core of the disk is dominated by

subsonic turbulence. The velocities become nearly supersonic above roughly $3 H_z$, the height at which the buoyant magnetic energy dissipates. In this region, shocks with Mach numbers as high as 2.9 are observed. These high velocities form as acoustic waves generated by the MRI carry part of the energy generated in the disk into the corona, steepening into shocks and dissipating there. The corona is not turbulent, but is highly dynamic.

It is interesting to ask whether largescale magnetic field structure is generated in the corona as it becomes magnetized. Figure 5 is a plot of the relative strengths of each component of the field energy. With the onset of the MRI, the energy in all three field components increases. However, it is clear that within both the disk and the corona B_y^2 dominates; it is more than an order of magnitude stronger than either of the other two components in both regimes. This is not surprising since differential rotation favors the production of B_y . In the disk we find an ordering of $B_y^2 \approx 15B_x^2$ and $B_x^2 \approx 2B_z^2$; this is consistent with previous three-dimensional studies of the MRI (e.g., HGB1, HGB2, and SHGB). Interestingly, the energy in the toroidal field is roughly equal in the disk and corona by the end of the run. This is due both to the efficiency of buoyancy in magnetizing the coronal region and to our shearing sheet boundary conditions which force Keplerian rotation and may thus be favoring the production of B_y . After only 10 orbital times the corona is fully magnetized; its configuration is roughly that of a well ordered, toroidal magnetic field. In the corona, B_x^2 and B_z^2 are approximately equal. Differential vertical velocities therefore increase B_z somewhat in the coronal region but are not enough to produce a strong B_z field here; the toroidal component of the field is larger than the poloidal by more than an order of magnitude. This differs slightly from the results of SHGB, who report an ordering of $B_x \approx 3B_z$ in both the corona and disk regions, suggesting the increase in the vertical domain of our simulations has allowed buoyant motions to develop more fully. We see largescale toroidal field configurations in both the corona and the disk, with small scale “wiggles” in the \hat{x} and \hat{z} directions. The slight secular decrease in the total disk magnetic energy is consistent with previous toroidal field studies; simulations on timescales longer than is possible here show the field never completely dies away.

3.1.1. Dissipation of Energy

Turning now to the resistive equivalent of our fiducial run (BYR1), we quantify the roles of dissipation and transport by examining the time rate of change of magnetic energy in the disk and coronal regimes. We use the fiducial resistive run for this analysis because we are able to explicitly measure resistive dissipation rates. In each of these volumes, magnetic energy is lost through a combination of the Poynting flux out of the volume and conversion into other forms of energy. Similarly, it is generated by conversion from other forms of energy (e.g. kinetic energy associated with the shear by the MRI) and the Poynting flux into the volume. If we let S_V denote the net generation of magnetic energy (embodying field generation by the MRI and energy loss due to conversion into other forms of energy), then we can write an equation of magnetic energy conservation as follows:

$$S_V = \frac{\partial \int_V (B^2/8\pi) dV}{\partial t} - \oint_S (B^2/4\pi) \mathbf{v} \cdot d\mathbf{S} + \frac{1}{4\pi} \oint_S (\mathbf{B} \cdot \mathbf{v}) \mathbf{B} \cdot d\mathbf{S} - \int_V \eta J^2 dV, \quad (8)$$

where the last term on the right indicates losses due to resistive heating and the second and third terms represent the Poynting flux out of the volume. We can characterize the

dissipation of energy throughout the volume by comparing the relative strengths of each of these components in the disk and coronal regimes. We will also compare with the heating rate due to compression and artificial viscosity, R_{heat} , given by:

$$R_{heat} = \int_V (P \nabla \cdot \mathbf{v}) dV + \int_V (\mathbf{q} \cdot \nabla \mathbf{v}) dV, \quad (9)$$

where the components of \mathbf{q} , given by

$$q_i = 4\rho(dv_i/dx_i)^2, \quad (10)$$

are the artificial viscous pressure used in the ZEUS code to capture shocks (thus the viscous heating as we have defined it includes shock heating), and we will compare with the flux of kinetic energy, F_{kin} :

$$F_{kin} = (1/2) \oint_S (\rho v^2) \mathbf{v} \cdot d\mathbf{S}. \quad (11)$$

We will report each quantity in units normalized by the initial pressure, P_o , per orbit. Time averages are computed for orbits 15-50, after saturation of the MRI. In addition, we have plotted the instantaneous net magnetic energy generation rate (S_V) in Figure 6 as a function of orbital time in the disk (left panel) and coronal (right panel) regions. In each plot, S_V has been averaged spatially within $\pm 2 H_z$ (left panel) and above $\pm 2 H_z$ (right panel) and normalized by the initial pressure, P_o .

In the disk, S_V has a net positive time-averaged value of 0.10, the average magnetic energy generation rate is ≈ -0.0005 , and the average Poynting flux out of the volume is 0.10. Resistive heating is very small, with an average value of 0.0023. In the disk, the evolution of the S_V term (see Figure 6a) is dominated by largescale ($\delta S_V \gg \langle S_V \rangle$) fluctuations; these are related to the production of field via the MRI and to the loss of flux via buoyancy. The net positive time average value of S_V indicates there is a local increase in magnetic energy within the disk. This agrees well with the results of SHGB (see their figure 11); they also found the evolution of S_V to be dominated by fluctuations and report a net positive value within the disk core. (The major difference is that we do not see their initial spike in S_V ; this is because we start with a toroidal magnetic field instead of a poloidal field). Our average value is more than an order of magnitude larger than that reported by SHGB, probably due to the fact that we measure S_V at two scale heights at the boundary between the turbulent core and stable corona, where buoyancy fluxes are a maximum (SHGB reported values measured at only one scale height).

Comparing generation and loss rates in the disk, we find that energy generation via viscous heating dominates. Loss of magnetic energy due to resistive heating is quite low, representing only 0.71 % of the viscous heating rate. The average Poynting flux out of the disk represents 30.9 % of the viscous heating rate while the flux of kinetic energy is only 5.03 % and has a net negative average (which represents flow into, not out of, the disk). Thus, the rate of energy loss as flux tubes rise out of the disk is about one quarter of the total disk energy generation rate. This shows that the MRI regenerates field quickly enough to ensure a net increase in magnetic energy and to sustain turbulence and angular momentum transport for the duration of the run in spite of significant field loss due to buoyancy. We also note that at two scale heights, the amount of magnetic energy lost via buoyancy is more significant than the value reported by SHGB at one scale height.

In the corona, the time average value for S_V is -0.012. The magnetic energy generation rate has an average of 0.0002, the net Poynting flux into the volume is 0.011 and the average

resistive heating is 0.00017. Comparing these values with those in the disk, we see that the situation in the corona is very different. The net Poynting flux rate is positive which means that more magnetic energy enters the corona than leaves it. However, the mean energy changes only slightly with time and the net value of the S_V term is negative. This indicates there is a local decrease in magnetic energy in the coronal region despite the net influx of field. We therefore conclude that the excess magnetic energy transported into the coronal region through the $z = \pm 2H_z$ boundaries is dissipated there. Looking at Figure 6b, we see that S_V shows large fluctuations; these correlate very well with the rise of flux tubes into the volume. The correlation of the net flux into the corona with the fluctuations in the net magnetic energy generation rate (the S_V term) indicates that transport of energy dominates local processes in the corona. Therefore, although there is a net transport of MRI generated flux into the corona, this region remains stable: no magnetic energy generation occurs and the net magnetic energy transported into the corona is dissipated there. We note that SHGB also report a net loss of field in the coronal region, although, as before, their net value for S_V is an order of magnitude smaller.

The energy in the net transported magnetic field is 60.1 % of the viscous heating in the coronal region; magnetic energy is thus the dominant form of heating here. However, it represents only 3.4 % of the viscous heating in the disk; therefore, it is only a small fraction of the overall energy budget. Resistive dissipation in the corona is surprisingly small. This is most likely due to the fact that the field structure is predominantly toroidal in both the disk and corona (as discussed above). Therefore, it is already fairly ordered as it rises into the corona. This also means that loss of magnetic energy in the coronal region is due more to its conversion into other forms of energy (e.g., kinetic energy) than to reconnection (as measured by η_o). The flux of kinetic energy is comparable in magnitude to the Poynting flux, although its average value is negative, indicating a net flow both back into the disk region and out of the upper boundary of the simulation (roughly 10 % of the kinetic flux escapes through the upper boundary). Thus, energy enters the corona mostly in the form of magnetic energy. We conclude that the heating of the corona occurs via the conversion of magnetic energy into kinetic energy which is then dissipated by the viscosity.

3.1.2. Effect of Resistivity and Resolution

The evolution described above is typical of all toroidal field runs. The resistive runs show growth due to the MRI at slightly later orbital times, but otherwise follow the same qualitative evolution. As we increase the resistivity (i.e. from $R_M = 20,000$ in run BYR1 to $R_M = 10,000$ in run BYR2), the effect increases (i.e., growth occurs at increasingly later orbital times), but the general evolution does not change. The delay in growth with the addition of resistivity occurs because resistivity tends to diffuse gradients in the field, resulting in damping of the fastest growing wavelengths (Sano et. al 1998; Fleming et. al. 1999).

Run BYR3 is a high resolution version of the fiducial resistive run (BYR1); it was run on a grid containing twice the standard resolution. Again, the qualitative evolution remains the same as that described above. Comparing over the same time periods, the post saturation volume averaged values of magnetic energy increase by a factor of 1.3 in the disk region and 1.8 in the coronal region. We find the same ordering in the relative strengths of the individual components of magnetic energy in both regions regardless of resolution (see Figure 5). The azimuthal components of both the Reynolds stress and Maxwell stress

increase with resolution by factors of 1.6-1.5 (respectively) in the disk region. In the corona, the azimuthal component of the Reynolds stress remains nearly the same, increasing by only a factor of 1.2 while that of the Maxwell stress increases by a factor of 1.5. Thus, doubling the resolution has made important differences to some components of the energy and stresses, but in all cases this difference is less than a factor of two. The increases in magnetic energy and stress are probably due to an increase in the range of MRI unstable wavenumbers which are resolved in the simulation. Overall, the α parameter increases by a factor of 1.5 in the disk as we double the resolution. Most importantly, plotting the equivalent of Figure 2 for run BYR3, we find the profiles of all four quantities to be almost identical. β spans the same range in values from the disk midplane to the corona, and mean magnetic and kinetic energy values are the same in both regions as are mean values of the azimuthal components of the Maxwell and Reynolds stresses. The only noticeable difference in the graphs is in the magnetic energy and the azimuthal component of the Maxwell stress; these both dip to lower values at the disk midplane in the standard resolution runs instead of remaining approximately constant throughout the disk as they do in the high resolution run. Again, this indicates that we may not be resolving all of the unstable wavelengths in the disk midplane in the standard resolution simulations. Shock and resistive heating remain the same as in the standard resolution runs. Poynting flux also remains the same over the entire grid while the flux of kinetic energy increases with resolution by factors of 4.8 in the disk and 2.0 in the corona. However, the velocity dispersion, which characterizes the turbulence of the flow, has the same profile and average values as in the standard resolution runs (see Figure 4). We find that the evolution of S_V in both the disk and the coronal regions is the same as that described above for the standard resolution runs. The average value of S_V in the disk increases by 15% in the high resolution run; the average coronal value remains unchanged. It appears that our standard resolution simulations capture the qualitative evolution very well, although they may underestimate some quantities, such as the α parameter.

We have also varied the initial field setup to ensure that our choice of $\pm 2 H_z$ as the initially magnetized region is not reflected in the results. We tried limiting this initially magnetized region to $\pm 1 H_z$ as well as holding \mathbf{B} constant within $\pm 2 H_z$, enforcing $\beta = 25$ at the equatorial plane only; these are also listed in Table 1 as BY2 and BY3, respectively. None of these changes resulted in any significant differences with the general evolution described above. Finally, we repeated the fiducial run doubling the radial domain (run BY4). The small radial extent of our simulations may be limiting the off-diagonal components of the stress tensor and thus the production of magnetocentrifugal winds. Our small radial domain size may also be limiting transport rates and fluxes. However, doubling the radial domain size was not enough to produce any significant difference. Magnetic energy and magnetic and kinetic stresses actually decreased (by factors of 1.1-1.2) in both the disk and coronal regions when the radial domain was doubled. This leads to a slight decrease in the α value for the disk in run BY4 (by a factor of 1.2) compared to the value in the fiducial run. The Poynting flux and flux of kinetic energy remained the same at both the disk surface ($\pm 2 H_z$) and the outer boundary of the simulation box. There was also no change in the net rate of generation of magnetic energy (the S_V term) in the coronal and disk regions. We did not continue increasing the domain size due to the amount of computational time required. Clearly, the most fruitful means of investigating these issues is to perform fully global simulations which span a large range in radii.

3.2. Zero Net Z Simulations

The Zero Net Z field simulations are identified in Table 1 by the prefix “ZN.” Our fiducial simulation (ZN1) is a standard resolution, nonresistive run with $\beta(0)=25$. The simulation was run for 50 orbital times. The critical wavelength for this run corresponds to $20.8 \Delta z$ (within the disk midplane); it is well resolved. Note that in SHGB this field configuration was the fiducial model. In this paper, we adopt toroidal field runs as the fiducial model both because a toroidal field configuration is physically motivated by the differential rotation of the disk and because we have to close B_z fieldlines in the coronal region, producing curved field lines there. (This was not an issue for the models presented in SHGB since they used periodic boundary conditions at $\pm 2H_z$.) The primary effect of the curvature of the field lines in the upper layers of the disk is to create tension forces which cause motions in the low density regions long before the MRI has saturated in the disk midplane.

Despite the change in initial magnetic field configuration, the qualitative evolution of the ZNZ runs is very similar to that of the toroidal field simulations (described above). As expected (see HGB1, HGB2, SHGB), the MRI emerges earlier (after only 2-3 orbits) than in the toroidal field runs. Figure 7 is a space-time plot of run ZN1 showing the vertical variation of horizontally averaged magnetic energy (top panel), the azimuthal component of Maxwell stress (2nd panel), kinetic energy (3rd panel), and the azimuthal component of Reynolds stress (bottom panel) versus orbital time. The MRI develops initially in the upper layers of the disk. By three orbits, however, the dominant modes are those at the disk midplane. As in the toroidal field runs, the MRI increases the magnetic energy within the disk region, and the magnetic energy rises buoyantly into the corona. Strongly magnetized regions rise with approximately the same slope (as measured in the space-time plots) as in the toroidal field runs and saturate at $3 H_z$, creating a magnetized corona. As in the toroidal field simulations, this process is periodic on a short (3-4 orbit) timescale. The major difference between run ZN1 and the toroidal field runs is that here the instability appears to die away at the midplane at the end of the run; the average value of β at the midplane at late times yields a ratio of $\lambda_c/\Delta z = 5.9$, indicating that the critical wavelengths are just barely resolved.

The main quantitative differences between the ZNZ and the toroidal field simulations lie in the magnetic quantities, which are uniformly smaller in the ZNZ runs. This is most likely due to the fact that the critical wavelengths are not well resolved in the midplane by the end of the ZNZ simulations. Figure 8 shows the horizontally averaged values of the density, β , kinetic and magnetic energies, and the azimuthal components of the Maxwell and Reynolds stresses averaged over orbits 10-50, after saturation of the MRI. Comparing Figure 8 with Figure 2, we see that the range in density is approximately the same for both field configurations. The average coronal values of β are about the same, although β is 6 times larger in the midplane in the ZNZ run, so that it spans slightly more than 4 decades over the vertical extent of the grid. The range in the azimuthal component of the Maxwell stress is about the same in both runs, although the absolute values are smaller in the ZNZ field runs. Probably the most notable feature of the profiles is a sharp dip at the midplane in both the magnetic energy and the azimuthal component of Maxwell stress. This is largely due to the strong transient burst of magnetic energy that occurs around $2 H_z$ between orbits 30 and 40 (see Fig. 7). The kinetic energy follows the density profile closely and has about the same range as in the toroidal field runs. The azimuthal component of the Reynolds stress drops more sharply in the disk surface layers and corona compared to the toroidal field runs, although it spans approximately the same range. The disk α parameter for this field configuration is about 0.01, which is about a factor of 3 smaller than the

value found in the toroidal field runs. We assign no significance to the dip in the magnetic quantities at the midplane (since it is caused by a transient feature); neglecting the dip, the profile of the stress for these runs follows the form we found for the toroidal field runs; i.e., it is approximately flat within the disk core and is proportional to the density in the corona.

In spite of its initially vertical structure, the field within the disk becomes predominantly toroidal due to differential rotation before beginning its buoyant rise and is thus toroidal in the coronal region as well (see Figure 9). Comparing Tables 2 and 3, we find the same relative ordering of the components of magnetic energy in both the disk and coronal regions as we did in the toroidal runs (see Figure 5 for comparison). The ordering of the kinetic energies in both the disk and coronal regions is also the same as in the toroidal field runs. As before, all quantities show large fluctuations.

We find that energies and stresses are generally slightly lower in the ZNZ simulations than in the toroidal runs. Magnetic energies in the disk are factors of 3-4 lower in the ZNZ runs, and in the corona factors of 2-3 lower. Surprisingly, even the energy in the \hat{z} component of the field are lower in the ZNZ field simulations, in spite of the initial vertical field configuration. Kinetic energies are lower by factors of 2-3 in the disk and 1-2 in the corona. Magnetic and kinetic stresses are also lower, with ZNZ values averaging 4 (2) times smaller in the disk for the magnetic (kinetic) quantities and 3 times smaller in the coronal region for both magnetic and kinetic quantities. Two notable exceptions are the $-B_x B_z$ term, which is nearly identical in the coronal region to the toroidal field value, and the coronal value of the $-B_y B_z$ term, which is almost a factor of 10 smaller for the ZNZ field simulations. We find an α parameter of .0079 for our fiducial ZNZ run; this about a factor of 3 smaller than that cited for the toroidal field simulations ($\alpha = 0.027$). The $B_y B_z$ and $B_x B_z$ components of the stress tensor show a much stronger correlation with the rising magnetic flux tubes described above, indicating this field configuration may be more favorable to the production of ordered stress patterns which can fuel magnetocentrifugal winds; however, their time averaged values are still very low ($7.2 \times 10^{-5} P_o$ for the $B_y B_z$ component) in this region. Magnetic fluxes are roughly a factor of 3 smaller than those measured in the toroidal field runs; kinetic fluxes are factors of 2-3 smaller. However the ratios of flux to energy for both magnetic and kinetic quantities are approximately the same; this may explain why the coronal field geometry at saturation is identical to that seen in the toroidal field runs. Overall, there are surprisingly few qualitative differences between simulations run with ZNZ and toroidal initial field configurations, although most quantities are slightly lower in the ZNZ runs.

We note that we repeated run ZN1 with resistivity (run ZNR1), using $R_M = 20K$ as in the fiducial resistive toroidal field simulation. We find that the effects of resistivity on the ZNZ simulations is the same as that discussed above for the toroidal field simulations. (See Fleming et. al. (1999) for a more complete discussion of the effect of resistivity on different initial field configurations.)

3.3. Pure B_z Simulations

The evolution of a pure B_z field geometry is interesting because it is relevant to a circumstellar disk threaded by a stellar magnetic field; i.e., a disk with a net vertical flux. Although far from the central star the stellar field is likely to be dipolar, in the local approximation adopted here we represent the stellar field as a uniform strength B_z field.

These simulations are listed in Table 1 with the identifier "BZ." Our fiducial simulation (BZ1) is a standard resolution, nonresistive run with $\beta(0) = 25$. This simulation has been run for 15 orbital times. However, we will only discuss the evolution up to 5 orbital times; beyond this point, the disk geometry is destroyed and the grid becomes magnetically dominated everywhere. The shearing sheet boundary conditions, which enforce Keplerian rotation everywhere, are then no longer appropriate for following the further evolution.

Figure 10 is a space-time plot showing the vertical variation of horizontally averaged magnetic energy (top panel), the azimuthal component of Maxwell stress (2nd panel), density (3rd panel), and the azimuthal component of Reynolds stress (bottom panel) versus orbital time (along the \hat{x} axis). It is immediately obvious from a comparison of Figure 10 with Figures 1, 3, and 7 that the evolution of a uniform B_z field is completely different from that of the other field geometries discussed in this paper. The difference is due to the development of the axisymmetric phase of the MRI known as the channel solution (Hawley & Balbus 1991; Goodman & Xu 1994). The channel solution develops at about 3 orbits; it is characterized by exponential growth of the magnetic field which causes the disk to separate vertically into horizontal planes (axisymmetric "channels" - see panel 3 of Figure 10). Note that the magnetic energy and the azimuthal components of the Maxwell stress are large in the regions between the channels; these rise due to a combination of magnetic buoyancy and pressure. The uppermost of these channels rise out of the simulation box in less than 1 orbital time (these can just barely be seen rising from the low density surface layers of the disk). The rise of the channels which originate closer to the midplane is checked by the onset of the Parker instability, which causes undulations in the rising density channels. Mass slides along the bends in the channels back towards the midplane, reforming a semblance of a disk structure which oscillates about the midplane before reaching an equilibrium state. The simulation is magnetically dominated everywhere by the end of the run.

Figure 11 is a snapshot of the vertical structure at 5 orbits, after the disk has been reformed. The quantities in Figure 11 have been averaged spatially in the horizontal directions. The plot of density shows that the bulk of the disk is at the midplane, although its initial symmetric structure has been perturbed. The plot of β indicates that both the disk and the coronal regions are magnetically dominated; $\beta \lesssim 1.0$ everywhere. We see from the plot of magnetic energy that the field has become very large at the midplane; it is of the same order of magnitude as the kinetic energy in the disk and is suprathermal over the entire grid. This is very different from the toroidal field runs (see Figure 2), where the disk field remained subthermal throughout the evolution. The strong magnetic pressure at the midplane drives the asymmetric density distribution. The plot of the azimuthal components of the stresses indicates that the Maxwell term dominates over the Reynolds term everywhere, and that the Maxwell term varies by at most a decade over the entire grid. Thus, after the disk reforms, matter is highly magnetically dominated in both the disk and coronal regions. The field structure is tangled and complicated, with $B_y^2 \approx B_x^2 \approx B_z^2$ over the entire grid.

We have also completed runs in which the initial density profile is a function of x (BZ2) and of x & z (BZ3). Such density distributions seed faster growing modes of the Parker instability, allowing it to curb the violent rise of the buoyant channels more quickly. In these simulations, mass loss due to the channels is less; however, the general evolution is qualitatively similar to that described above.

We conclude that purely vertical fields quickly lead to a magnetically dominated disk everywhere. Simulations beginning with purely vertical fields were attempted by SHGB,

and similar evolution was noted, however because of the much smaller vertical domain used by these authors, the buoyant channels would hit the boundary at $\pm 2H_z$ before the Parker instability could grow. Further simulations of this initial field geometry will require global models in order to capture the dynamics of the strongly magnetized regions properly (without enforcing Keplerian rotation).

4. Discussion

In this paper, we have shown that the evolution of a weakly magnetized stratified disk is characterized by the generation of magnetic field via the MRI and the loss of magnetic field through the buoyant rise of flux tubes (as long as the channel solution is not excited). The magnetic energy of buoyantly rising field saturates at about 2.5-3.0 H_z and thereafter dissipates, serving to both magnetize and heat the corona (the region above $\pm 2H_z$). The presence of a hot corona above an accretion disk has important observational consequences, as discussed in the introduction. It is therefore interesting to quantize the dissipation of total energy ($E_{tot} = E_{mag} + E_{kin} + E_{th}$) as a function of height above the disk and to use this to calculate a thermal equilibrium temperature profile in the corona assuming the heating rate is balanced locally by optically thin cooling. In this section, we will estimate the coronal temperature distribution for two important cases: 1) a protostellar disk around a CTTS and 2) a disk around a neutron star, and compare our results with the coronal temperatures measured by observations.

We first examine the case of a typical protostellar disk. In order to convert quantities measured in our simulations into physical units, we adopt the average CTTS parameters found in Beckwith et. al. (1993) (i.e., mass of disk $\approx 0.03M_\odot$; radius of disk $\approx 50AU$). We assume our simulation box is located at $R = 3R_*$ (the inner edge of the disk) and that within two scale heights the disk is optically thick and has a temperature of 1000 K. The total dissipation rate as a function of vertical height, D , we approximate as:

$$D(z) = R_{heat} + \left(\oint_S \eta J^2 dx dy \right) \times \Delta z, \quad (12)$$

where R_{heat} is as defined in equation [9] (except here we integrate over a differential volume (corresponding to a horizontal plane with a height of one grid zone) instead of the entire simulation domain), and each quantity in the sum is averaged over horizontal planes at each vertical position in the numerical grid, and also averaged over time. We convert the total dissipation rate into an average per particle heating rate, Γ , in $\text{erg cm}^2 \text{ s}^{-1}$ via

$$\Gamma = D / (\epsilon V \bar{n}^2), \quad (13)$$

where ϵ is a dimensionless heating efficiency and \bar{n} is the average number density of particles within the volume V . We find that the shock heating term dominates the other dissipative components in our simulations; because it tends to be strongly localized, we set $\epsilon = 10^{-3}$. To be consistent with our definition of D , the volume V is the planar area $\Delta x \Delta y$ times dz , where dz is the height of a vertical grid zone in units of H_z . To compute the equilibrium temperature, we equate the per particle heating rate with an optically thin cooling rate, Λ , and solve for the temperature T . Using data from run BYR1, averaged over orbits 15 through 50, we find the profile shown in Figure 12, where we have used the cooling rate given in figure 2 of Dalgarno & McCray (1972, hereafter DM) to yield the temperature

scale. Note that our assumption of a disk temperature at $\pm 2H_z$ of $T(\pm 2H_z) \sim 1000K$ is at least consistent with our result. In calculating the temperature at this point, we have used the curve in DM corresponding to the highest degree of ionization. This seems reasonable in the low density coronal regions; however, we note that different assumptions about the degree of ionization at $2H_z$ would lead to a different temperature for the same amount of dissipation.

The thermal equilibrium temperature is of order 10^4 K in the coronal region. This is consistent with the warm temperatures Kwan et. al. (1997) need to account for the O I and Balmer lines of CTTS. For comparison, we apply our model to the case of 1548C27, using the stellar parameters given by Najita et. al. (1996). Assuming we are at their fiducial radius, we find a temperature $\approx 9,000$ - $10,000$ K for the inner disk atmospheric temperature. This is consistent with the temperature they derive to model the CO overtone emission in this star. Since our simulations are local, we cannot meaningfully compute a radial temperature profile for the corona to compare to their data. We emphasize that the fluctuations in D about the mean value are large (factors of 4) which implies that the heating rate and peak temperatures in the corona will be highly time dependent. We find the temperature can vary by as much as two orders of magnitude on short ($t \ll t_{orb}$) timescales. Thus, our simulations show that a turbulent protostellar accretion disk produces a nonturbulent, magnetized, warm ($T \sim 10^4$) corona, with short timescale temperature fluctuations.

We now turn to the case of an accretion disk surrounding a compact object. Adopting typical values of $1.0 M_\odot$ for the mass of the neutron star, 10^8 cm for a representative disk radius, and $\dot{M} = 1.6 \times 10^{-9} M_\odot \text{yr}^{-1}$ as a typical accretion rate, we can use the formulae in Lovelace et. al. (1995) to derive a fiducial disk mass, velocity, and time. These allow us to convert the total dissipation rate into the per particle heating rate, Γ , as before. Using the neutron star parameters and comparing with the cooling rate given in figure 1 of Raymond et. al. (1975), we find that a typical thermal equilibrium temperature in the corona is of order 10^8 K at $3H_z$, which is in the X-ray range. Thus, we find the amount of energy generated by the MRI in the midplane of the disk and transported into the corona via buoyancy is sufficient to heat the corona to temperatures inferred from observations for disk coronae around compact objects.

It is encouraging that the estimates presented in this section are consistent with temperatures suggested by current observational data as well as numerical calculations. However, we caution that there are many uncertainties in our estimates, most particularly in our choice of ϵ , which, although motivated by the strong dominance of shock heating in our simulations, was admittedly ad hoc. If the heating were less localized, ϵ could be as high as 1.0, which would change the temperature range significantly.

5. Conclusions

We have performed quasi-global MHD simulations of the dynamical evolution of vertically stratified accretion disks which demonstrate the generation of a magnetized corona. Initially weak magnetic fields in the core of the disk (below two scale heights) are amplified via MHD turbulence driven by the MRI. This field becomes buoyant and rises out of the disk. The magnetic energy density associated with buoyantly rising magnetic field peaks at about 2.5-3.0 H_z and then dissipates, creating a magnetized, heated coronal

region above the disk core. We show that this process is highly time-dependent; throughout our simulations, the accretion disk continues to generate field via the MRI, which leads to the rise of flux out of the disk and its subsequent dissipation in the corona. On long time-averages, the vertical structure of the disk is a turbulent core which is unstable to the MRI surrounded by a highly dynamic, magnetically dominated ($\beta \lesssim 10^{-1}$), heated, stable corona. The largescale field configuration in both the disk and the coronal region is toroidal. Our simulations are the first to follow the highly coupled amplification, buoyant transport, and saturation processes which control the magnetic field, as well as the angular momentum transport process which controls the disk, from first principles.

We have characterized the dissipation of energy as a function of vertical height for these simulations. We find that local processes dominate over transport in the disk region. This leads to heating of the disk by turbulence and to the continuation of angular momentum transport via the MRI throughout the simulations. In the coronal region, however, transport processes dominate because it is strongly magnetized ($\beta < 1.0$) and therefore stable to the MRI. Shocks with Mach numbers as high as $M \approx 2.9$ are observed in the corona throughout the evolution; these are produced both by the steepening of MHD waves associated with the turbulence in the disk as they propagate into the low density corona, and via mass motions into the corona itself. By equating the time-averaged per particle heating rate in the corona with an optically thin cooling rate, we estimate the equilibrium temperature of the corona is of order 10^4 K for a typical accretion disk around a CTTS, and of order 10^8 K for a disk around a typical neutron star, although there is considerable uncertainty in these estimates. We note that the temperature can vary by as much as two orders of magnitude on short ($t \ll t_{orb}$) timescales. The functional form of the stress as a function of vertical height is flat within $\pm 2H_z$ but falls off proportional the density (i.e., as a Gaussian) above $\pm 2H_z$.

We find that these results are general in the sense that they do not depend on resolution, resistivity (so long as the MRI is not quenched), nor initial field configuration (as long as the axisymmetric linear phase (the channel solution) of the MRI is not excited). They do depend on the initial field strength (if the field is strong, $\beta > 1.0$, and the disk becomes MRI stable). They may also be affected by the vertical structure of the disk. We assume an isothermal profile in all the simulations presented here; adiabatic disks may not be as strongly stratified and this may affect the buoyant transport rates. We are also limited by the use of the local approximation in the plane of the disk, which enforces Keplerian rotation everywhere, including in the strongly magnetized corona. This may suppress the generation of MHD winds. Extending our models to be global in all three directions is the natural next step in this study.

We have also presented simulations in which the axisymmetric linear phase of the MRI is excited. Unlike the evolution described above, these simulations are dominated by the formation of density channels, which rise quickly out of the disk due to a combination of magnetic buoyancy and pressure. The rising density sheets are subject to the Parker instability, which results in mass sliding back to the midplane to reform a disk structure. This highly dynamic evolution may be relevant to the processes by which a stellar magnetic field can disrupt an accretion disk within the star-disk interaction region.

We thank Steve Balbus for suggesting improvements to the Alfvén speed limiter algorithm, and John Hawley and the referee (Ulf Torkelsson) for useful comments. This work was supported by the NSF through grant AST95-28299.

A. Large Alfvén Speed Limiter via the Displacement Current

An important aspect of this work is the extension of the simulation domain to include ten vertical scale heights (five above and five below the disk midplane). In time explicit codes such as ZEUS, the time step is constrained in part by the shortest crossing time of an Alfvén wave across a grid zone. Thus, low density regions (such as those three to five H_z above the disk midplane) where the Alfvén speed becomes unmanageably large must be avoided. In the current simulations, we are able to work in the low density coronal region through the addition of the displacement current in the equation of motion [2], combined with a artificially low value for the speed of light c . This method was first used by Boris (1970) (see also the review by Brecht 1985).

In practice, we set $c = c_{lim}$ (an arbitrary scaling speed) in the displacement current term in equation [2], which constrains v_A/c_{lim} to be $\lesssim 1$. We can thus choose c_{lim} such that $\Delta x/v_A$ is a reasonable value everywhere in the simulation domain. In this work, we choose c_{lim} such that it is always approximately an order of magnitude greater than the (isothermal) sound speed; $c_{lim} = 5.66 \times 10^{-3}$. This ensures that we allow a good dynamical range in the runs; i.e., the Alfvén speed and the sound speed are allowed to differ significantly. It also makes our omission of relativistic terms introduced by the displacement current reasonable (i.e., $v_A/c_{lim} \lesssim 1$, but in general $v/c_{lim} \ll 1$, where v represents the other velocities in the simulation). We also note that we have tested the effect of this limiter by varying it over a range of values up to the value we report in this paper (compare columns 8, 9, & 10 of Table 1 for runs BY5, BY6, & BY1 and ZN2 & ZN1). As c_{lim} is increased, the only effect is an increase in the coronal kinetic energies and stresses. This is not unexpected, since we are limiting magnetic stresses, and therefore velocities, in the coronal region through the use of c_{lim} . The amplitudes of the magnetic energy are not significantly changed.

Our derivation proceeds as follows. Consider the momentum equation:

$$\rho \frac{\partial \mathbf{v}}{\partial t} + \rho \mathbf{v} \cdot \nabla \mathbf{v} = -\nabla P + \frac{1}{c} (\mathbf{J} \times \mathbf{B}), \quad (\text{A1})$$

where vertical gravity and the shearing box rotational terms have been omitted. The displacement current enters through the definition of the current:

$$\mathbf{J} = \frac{c}{4\pi} [\nabla \times \mathbf{B} - \frac{1}{c} \frac{\partial \mathbf{E}}{\partial t}] + \xi^+ \mathbf{v}, \quad (\text{A2})$$

where \mathbf{E} is the electric field and ξ^+ is the charge density. The last term represents the electric field force on the plasma. We can self-consistently include it in the definition of the current because it does not affect the energy balance in the code (e.g., $\mathbf{v} \times \mathbf{B} \sim \mathbf{E}$, and $\mathbf{v} \cdot \mathbf{E} = 0.0$). The motivation for choosing this form for \mathbf{J} will become apparent below.

Assuming infinite conductivity², \mathbf{E} is given by the usual Ohm's law. Substituting in for

²We note that the terms introduced by including a finite conductivity are of order $v/c \ll 1$; thus, we can self consistently assume infinite conductivity in Ohm's law.

\mathbf{J} , we find:

$$\rho \frac{\partial \mathbf{v}}{\partial t} + \rho \mathbf{v} \cdot \nabla \mathbf{v} = -\nabla P + \frac{1}{4\pi} (\nabla \times \mathbf{B}) \times \mathbf{B} - \frac{1}{4\pi c} \frac{\partial \mathbf{E}}{\partial t} \times \mathbf{B} + \frac{\xi^+}{c} (\mathbf{v} \times \mathbf{B}). \quad (\text{A3})$$

Substituting in for \mathbf{E} and rearranging leads to:

$$\rho \frac{\partial \mathbf{v}}{\partial t} + \rho \mathbf{v} \cdot \nabla \mathbf{v} = -\nabla P - \nabla \frac{B^2}{8\pi} + \frac{1}{4\pi} (\mathbf{B} \cdot \nabla) \mathbf{B} + \frac{1}{4\pi c^2} \frac{\partial (\mathbf{v} \times \mathbf{B})}{\partial t} \times \mathbf{B} + \frac{\xi^+}{c} (\mathbf{v} \times \mathbf{B}). \quad (\text{A4})$$

We use the induction equation to bring \mathbf{B} into the time derivative in the penultimate term on the right:

$$\rho \frac{\partial \mathbf{v}}{\partial t} + \rho \mathbf{v} \cdot \nabla \mathbf{v} = -\nabla P - \nabla \frac{B^2}{8\pi} + \frac{1}{4\pi} (\mathbf{B} \cdot \nabla) \mathbf{B} + \frac{1}{4\pi c^2} \frac{\partial (\mathbf{Q} \times \mathbf{B})}{\partial t} - \frac{1}{4\pi c^2} \left[\frac{1}{2} \nabla Q^2 - (\mathbf{Q} \cdot \nabla) \mathbf{Q} \right] + \frac{\xi^+}{c} \mathbf{Q}, \quad (\text{A5})$$

where $\mathbf{Q} = \mathbf{v} \times \mathbf{B}$. We wish to write the penultimate term on the right as the divergence of a tensor to guarantee conservation of angular momentum. Because $\nabla \cdot \mathbf{Q} \neq 0.0$, we must add (and subtract) $\frac{1}{4\pi c^2} \mathbf{Q} \nabla \cdot \mathbf{Q}$ to do this. Then, using the equation of mass conservation to bring ρ into the time derivative on the left, we find:

$$\frac{\partial \rho \mathbf{v}}{\partial t} = -\nabla \cdot \overline{\overline{P}} - \nabla \cdot \overline{\overline{P_D}} + \frac{1}{4\pi c^2} \frac{\partial (\mathbf{Q} \times \mathbf{B})}{\partial t} - \frac{\xi^+}{c} \mathbf{Q} - \frac{1}{4\pi c^2} \mathbf{Q} \nabla \cdot \mathbf{Q} + \frac{\xi^+}{c} \mathbf{Q}, \quad (\text{A6})$$

where

$$P_{ij} = (P + \frac{B^2}{8\pi}) \delta_{ij} + \rho v_i v_j - \frac{B_i B_j}{4\pi}, \quad (\text{A7})$$

and

$$P_{Dij} = \frac{1}{4\pi c^2} [Q_i Q_j - \frac{|Q|^2}{2} \delta_{ij}]. \quad (\text{A8})$$

Note that the extra term we added to the current (the last term in eq. (A6)) exactly cancels the non-conservation term introduced in writing $\nabla \cdot \overline{\overline{P_D}}$. This justifies the definition of the current in eq. (A2).

We will now neglect the $\overline{\overline{P_D}}$ terms, which are of order $v/c \ll 1$. (Note that we can not simply drop the $\frac{\xi^+}{c} \mathbf{Q}$ term - even though it is of the same order of magnitude as the $\overline{\overline{P_D}}$ terms - because it is needed for conservation. This is especially important for the current study because of the key role angular momentum plays in the disk evolution which is driven by the MRI.) Canceling these terms, we then combine the time derivatives and write the mass density as a generalized tensor:

$$\rho_{ij}^* = (\rho + \frac{B^2}{4\pi c^2}) \delta_{ij} - \frac{B_i B_j}{4\pi c^2}, \quad (\text{A9})$$

to obtain

$$\frac{\partial (\rho^* \cdot \mathbf{v})}{\partial t} = -\nabla \cdot \overline{\overline{P}}. \quad (\text{A10})$$

The addition of the displacement current enters the momentum equation only via the mass density. We apply this change to the ZEUS code by replacing ρ with ρ^* for the pressure (gas + magnetic) source terms. We then rederive the equations of MOC, following the method outlined in Hawley & Stone (1995; hereafter HS) for the 1.5 D system. There is no explicit change in the induction equation. For the momentum equation, if we ignore the pressure terms and the off-diagonal terms in the modified mass density, we are left with

$$\frac{\partial \rho^* \mathbf{v}}{\partial t} = -\nabla \cdot (\rho \mathbf{v} \mathbf{v}) + \frac{1}{4\pi} (\mathbf{B} \cdot \nabla) \mathbf{B}, \quad (\text{A11})$$

which simplifies to

$$\frac{\partial \rho^* (v_x \hat{x} + v_y \hat{y})}{\partial t} = -\frac{\partial \rho v_x (v_x \hat{x} + v_y \hat{y})}{\partial x} + \frac{1}{4\pi} B_x \frac{\partial B_y}{\partial x} \hat{y} \quad (\text{A12})$$

for the 1.5 D system. The \hat{x} direction represents only the advection of momentum. For the \hat{y} direction, after a little algebra and making use of the fact that terms of order $v/c \ll 1$, we can write:

$$\rho^* \frac{\partial v_y}{\partial t} = -\rho^* v_x \frac{\partial v_y}{\partial x} + \frac{1}{4\pi} B_x \frac{\partial B_y}{\partial x}. \quad (\text{A13})$$

Comparing with equation (3.13) of HS, we see that the addition of the displacement current requires only that we replace ρ with $\rho^* = (1 + \frac{B^2}{4\pi \rho c_{lim}^2})\rho$ (where “c” has been replaced with the limiter “ c_{lim} ”) in the MOC equations.

We note that some of the simulations reported in this paper do not include the $\xi^+ \mathbf{v}$ term in eq. [A2]. We find that these runs show the same initial linear growth and saturation amplitude of the MRI as the simulations which do include this term. There is some indication that the long-term averaged values of the magnetic quantities (e.g., the magnetic energy) are slightly larger when this term is included. However, the large fluctuations which result from the chaotic nature of the MRI turbulence can lead to even larger differences in averaged quantities depending, e.g., on the time domain used in forming the average. Thus, averages must be performed over several hundreds of orbital times before secular differences in time averaged quantities can be considered meaningful. This suggests that the difference in the long-term average of the magnetic energy described above (where “long-term” refers to averages over < 50 orbits) is not significant. We stress that the presence of this term has no effect on the qualitative evolution discussed in the paper nor on the globally averaged quantities, such as the vertical profiles (see figs 2, 8, and 11). There are also no differences in the kinetic energies, stresses, or fluxes. The small increase in the time averaged value of the magnetic energy leads to a 3 % increase in the percent of energy dissipated in the coronal region (i.e., the Poynting flux increases as the magnetic field strength in the disk increases). However, we find that a different set of initial (random) perturbations can lead to differences of order 10 % in the solution (again due to the chaotic nature of the turbulence produced by the MRI) and therefore we do not assign any importance to this 3 % difference. In spite of the lack of evidence that the inclusion of the $\xi^+ \mathbf{v}$ term in eq. [A2] produces any real change in the results, we choose to include it in the fiducial toroidal (BY1) and ZNZ (ZN1) field simulations in order to strictly conserve angular momentum. We note that the other runs cited in this paper do not include this term.

REFERENCES

Balbus, S.A. & Hawley, J.F., 1998, Rev. Mod. Phys., 70, 1.

Basu, S., Mouschovias, T. C., & Paleologou, E.V., 1997, Ap.J., 480, L55.

Beckwith, S.V.w. & Sargent, A. I., 1993, in *Protostars and Planets III*, ed. Eugene H. Levy & Jonathan I. Lunine (Tucson: University of Arizona Press), 521.

Brandenburg, A., 1998, in *Theory of Black Hole Accretion Disks*, ed. Marek A. Abramowicz, Gunnlaugur Bjornsson, & James E. Pringle (Cambridge University Press), 61.

Brandenburg, A., Nordlund, A., Stein, R.F., & Torkelsson, U., 1995, Ap.J., 446, 741 (BNST).

Breth, S.H., 1985, Space Sci. Rev., 42, 185.

Boris, J.P., 1970, Naval Res. Lab. Memo. Rept. No. 2167.

Chou, W., Tajima, T., Matsumoto, R., & Shibata, K., 1997, P.A.S.J., 49, 389.

Coroniti, F.V., 1981, Ap.J., 244, 587.

Dalgarno, A. & McCray, R.A., 1972, A.R.A.A., 10, 375 (DM).

D'Alessio, P., Canto, J., Calvet, N., & Lizano, S., 1998, Ap.J., 500, 411.

Dove, J.B., Wilms, J., & Begelman, M.C., 1997, Ap.J., 487, 747.

Fleming, T.P., Stone, J.M., & Hawley, J.F., 1999, in press.

Galeev, A.A., Rosner, R., & Vaiana, G.S., 1979 Ap.J., 229, 318.

Goodman, J. & Xu, G., 1994, Ap.J., 432, 213.

Haardt, F., & Maraschi, L., 1991 Ap.J., 380, L51.

Hawley, J.F. & Balbus, S. A., 1991, Ap.J., 376, 214.

Hawley, J.F., Gammie, C.F., & Balbus, S.A., 1995a, Ap.J., 440, 742 (HGB1).

Hawley, J.F., Gammie, C.F., & Balbus, S.A., 1995b, Ap.J., 464, 690 (HGB2).

Hawley, J.F. & Stone, J.M., 1995, Computer Physics Communications, 89, 127 (HS).

Jackson, J.D., 1975, *Classical Electrodynamics*, (New York, John Wiley & Sons, Inc.), 218.

Kaisig, M., Tajima, T., Shibata, K., Nozawa, S., & Matsumoto, R., 1990, Ap.J., 358, 698.

Kamaya, H., Horiuchi, T., Matsumoto, R., Hanawa, T., Shibata, K., & Mineshige, S., 1997, Ap.J., 486, 307.

Kwan, J., 1997, in *Herbig-Haro Flows and the Birth of Stars*, Proceedings of IAU Sym. 182, ed. by B. Reipurth & C. Bertout, Kluwer, 443.

Liang, E.P.T. & Price, R.H., 1977, Ap.J., 218, 247.

Liang, E.P.T. & Thompson, K.A., 1979, M.N.R.A.S., 189, 421.

Lovelace, R.V.E., Romanova, M.M., & Bisnovatyi-Kogan, G.S., 1995, M.N.R.A.S. 275, 244.

Matsumoto, R., Tajima, T., Shibata, K., & Kaisig, M., 1993, Ap.J., 414, 357.

Najita, J., Carr, J.S., Glassgold, A.E., Shu, F.H., & Tokunaga, A.T., 1996, Ap.J., 462, 919.

Nandra, K. & Pounds, K.A., 1994, M.N.R.A.S., 268, 405.

Raymond, J.C., Cox, D.P., & Smith, B. W., 1975, Ap.J., 204, 290.

Sakimoto, P.J. & Coroniti, F.V., 1989, *Ap.J.*, 342, 49S.
Sakimoto, P.J. & Coroniti, F.V., 1981, *Ap.J.*, 247, 19S.
Sano, T., Inutsuka, S.-I., & Miyama, S.M., 1998, *Ap.J.*, 506, L57.
Shakura, N.I. & Sunyaev, R.A., 1973, *A & A*, 24, 337.
Stella, L. & Rosner, R., 1984, *Ap.J.*, 277, 312.
Stone, J.M., Hawley, J.F., Gammie, C.F., & Balbus, S.A., 1996, *Ap.J.*, 463, 656 (SHGB).
Stone, J.M. & Norman, M.L., 1992a, *Ap.J. Supp.*, 80, 753.
Stone, J.M. & Norman, M.L., 1992b, *Ap.J. Supp.*, 80, 791.
Torkelsson, U., 1993, *A & A*, 274, 675.
Tout, C.A. & Pringle, J.E., 1992, *M.N.R.A.S.*, 259, 604.
Wade, R.A., & Hubeny, I., 1998, *Ap.J.*, 509, 350.
Wood, D.T., Klein, R.I., Castor, J.I., McKee, C.F., & Bell, J.B., 1996, *Ap.J.* 461, 767.
Yi, I., & Kenyon, S.J., 1997, *Ap.J.*, 477, 379.

Fig. 1.— Space-time plot showing the vertical distribution of the horizontally-averaged magnetic (top panel) and kinetic (bottom panel) energy as a function of time in the fiducial model BY1. The magnetic energy varies between 0.0 (black) and $0.846 P_o$ (red); the range in kinetic energy between 0.0 (black) and $1.24 P_o$ (red).

Fig. 2.— Vertical variation of horizontally and temporally averaged quantities in model BY1. The time average is constructed between orbits 25 through 50. The horizontal average is taken over the $\hat{r}\hat{\phi}$ plane as described in the text.

Fig. 3.— Space-time plot of $B_x B_y$ (top panel), $\rho v_x \delta v_y$ (2nd panel), $B_x B_z$ (3rd panel), and $B_y B_z$ (bottom panel) in model BY1. The maximum (minimum) value, colored red (purple), in each plot is 0.322 (-0.118) P_o , 0.132 (-0.055) P_o , 0.04 (-0.03) P_o , and 0.044 (-0.046) P_o , respectively.

Fig. 4.— Horizontally and temporally averaged velocity dispersion in run BY1, normalized by the sound speed.

Fig. 5.— Volume averaged B_y^2 (solid line), B_x^2 (dashed line), B_z^2 (dot-dashed line), normalized by P_o , within the disk (left panel) and the corona (right panel) for model BY1.

Fig. 6.— Net magnetic energy generation rate S_V in the disk (left panel) and the corona (right panel) in model BYR1. In both plots, S_V has been volume averaged and normalized by P_o .

Fig. 7.— Space-time plot of magnetic energy (top panel), $B_x B_y$ (2nd panel), kinetic energy (3rd panel), and $\rho v_x \delta v_y$ (bottom panel) in model ZN1. The magnetic energy varies between 0.0 (black) and $0.443 P_o$ (red), the kinetic between 0.0 (black) and 1.175 (red), $B_x B_y$ between $-0.021 P_o$ (purple) and $0.134 P_o$ (red), and ρv_x between $-0.030 P_o$ (purple) and $0.078 P_o$ (red).

Fig. 8.— Vertical variation of horizontally and temporally averaged quantities in model ZN1. The time average is constructed between orbits 10 through 50. The horizontal average is taken over the $\hat{r}\hat{\phi}$ plane as described in the text.

Fig. 9.— Volume averaged B_y^2 (solid line), B_x^2 (dashed line), B_z^2 (dot-dashed line), normalized by P_o , within the disk (left panel) and the corona (right panel) for model ZN1.

Fig. 10.— Space-time plot of magnetic energy (top panel), $B_x B_y$ (2^{nd} panel), density (3^{rd} panel), and $\rho v_x \delta v_y$ (bottom panel) in model BZ1. The magnetic energy varies between $0.51 P_o$ (black) and $28.74 P_o$ (red), the range in density is 0.0 (black) to 8.69 (red), $B_x B_y$ varies between $-1.23 P_o$ (black) and $20.93 P_o$ (red), and the range in $\rho v_x \delta v_y$ is $-5.1 P_o$ (black) to $62.47 P_o$ (red).

Fig. 11.— Horizontally averaged vertical structure at orbit 5 in model BZ1. The horizontal average is taken over the $\hat{r}\hat{\phi}$ plane as described in the text.

Fig. 12.— Vertical variation of coronal thermal equilibrium temperature for model BYR1 for the case of a CTTS.

TABLE 1:
Parameters of Numerical Simulations

Run ^a	$\beta(0)$	R_M	c_{lim}	Grid	λ_c/Δ	Orbits	$\langle \frac{B^2}{8\pi P(0)} \rangle^b$ ($\times 10^{-2}$)	$\langle \frac{-B_x B_y}{4\pi P(0)} \rangle^b$ ($\times 10^{-3}$)	$\langle \frac{\rho v_x \delta v_y}{P(0)} \rangle^b$ ($\times 10^{-3}$)
BY1	25	∞	$8 c_s$	$32 \times 64 \times 128$	8.31	50	8.66/4.16	23.6/4.33	5.83/0.59
BY2 ^c	25	∞	$8 c_s$	$32 \times 64 \times 128$	8.31	20	6.34/1.80	17.8/1.78	4.36/0.394
BY3 ^d	25	∞	$8 c_s$	$32 \times 64 \times 128$	8.31	20	2.61/1.06	7.12/1.43	2.19/0.220
BY4 ^e	25	∞	$8 c_s$	$64 \times 64 \times 128$	8.31	30	5.87/3.16	15.4/2.57	4.37/0.389
BY5	25	∞	c_s	$32 \times 64 \times 128$	8.31	50	5.31/3.10	13.7/3.72	3.51/0.147
BY6	25	∞	$4 c_s$	$32 \times 64 \times 128$	8.31	15	9.41/6.72	24.6/9.24	6.03/0.629
BYR1	25	20,000	$8 c_s$	$32 \times 64 \times 128$	8.31	50	5.69/3.19	14.3/3.17	3.87/0.434
BYR2	25	10,000	$8 c_s$	$32 \times 64 \times 128$	8.31	20	5.55/2.98	11.1/2.53	2.85/0.340
BYR3	25	20,000	$8 c_s$	$64 \times 128 \times 256$	16.61	20	10.9/6.17	35.3/3.97	8.58/0.582
ZN1	25	∞	$8 c_s$	$32 \times 64 \times 128$	20.8	50	2.20/1.28	0.49/0.15	0.23/0.021
ZN2	100	∞	c_s	$32 \times 64 \times 128$	10.38	30	0.372/0.313	0.533/0.600	0.269/0.045
ZNR1	25	20,000	$8 c_s$	$32 \times 64 \times 128$	20.8	15	0.486/0.131	0.858/0.242	1.29/0.046
BZ1	25	∞	$8 c_s$	$32 \times 64 \times 128$	20.8	15	179.2/101.3	907.0/557.2	56.9/12.0
BZ2	100	∞	c_s	$32 \times 64 \times 128$	10.4	10	88.1/42.6	308.0/115.5	35.5/6.99
BZ3	100	∞	c_s	$32 \times 64 \times 128$	10.4	10	103.4/50.1	278.2/105.2	31.4/2.60

^a Run labels: the first two letters give the initial field configuration (BY=toroidal field, ZN=zero-net-z field, BZ=pure z field). “R” identifies the resistive runs.

^b Volume and time averages begun at 15 orbits (BY6, where the average was begun at 10 orbits and ZNR1, where the average was begun at 5 orbits). The first number represents the average within $2 H_z$; the second represents the average for $|z| > 2H_z$. For the BZ runs, these numbers are volume averages only, computed at orbit 5.

^c In this run, field was initialized only within $\pm 1 H_z$

^d In this run, $\beta = 25$ at the equator; B was held constant within $\pm 2 H_z$

^e In this run, the \hat{x} direction was doubled without increasing the resolution: $x \in [-1, 1]$.

TABLE 2:
Volume and Time Averaged Quantities in Run BY1

Quantity f	$\langle f \rangle^a$ ($\times 10^{-2}$)	$\langle \delta f^2 \rangle^{1/2} a$ ($\times 10^{-2}$)	min f ^a ($\times 10^{-2}$)	max f ^a ($\times 10^{-2}$)
$B_x^2/8\pi P_o$	0.49/0.14	0.23/0.09	0.0/0.0	1.0/0.58
$B_y^2/8\pi P_o$	7.39/3.87	2.15/2.58	3.92/0.0	12.6/8.93
$B_z^2/8\pi P_o$	0.26/0.18	0.12/0.12	0.0/0.0	0.52/0.49
$-B_x B_y/4\pi P_o$	2.14/0.43	0.97/0.27	0.0/0.0	3.80/1.47
$-B_x B_z/4\pi P_o$	0.01/-0.003	0.10/0.04	-0.09/-0.16	0.16/0.20
$-B_y B_z/4\pi P_o$	-0.03/0.04	0.05/0.05	-0.30/-0.08	0.21/0.15
$\rho v_x^2/2P_o$	1.11/0.12	0.52/0.09	0.0/0.0	2.65/0.71
$\rho \delta v_y^2/2P_o$	0.65/38.8	0.28/20.0	0.0/0.0	1.22/88.3
$\rho v_z^2/2P_o$	0.57/0.08	2.43/0.06	0.0/0.0	1.23/0.29
$\rho v_x \delta v_y/P_o$	0.53/0.06	0.28/0.06	0.0/-0.17	1.36/0.31
ρ	64.0/0.71	0.37/0.26	63.6/0.314	64.8/1.28

^a The first number represents the average quantity f within $\pm 2H_z$; the second number represents the average quantity f for $|z| > 2H_z$. Averages have been taken over 25 orbital times, after saturation.

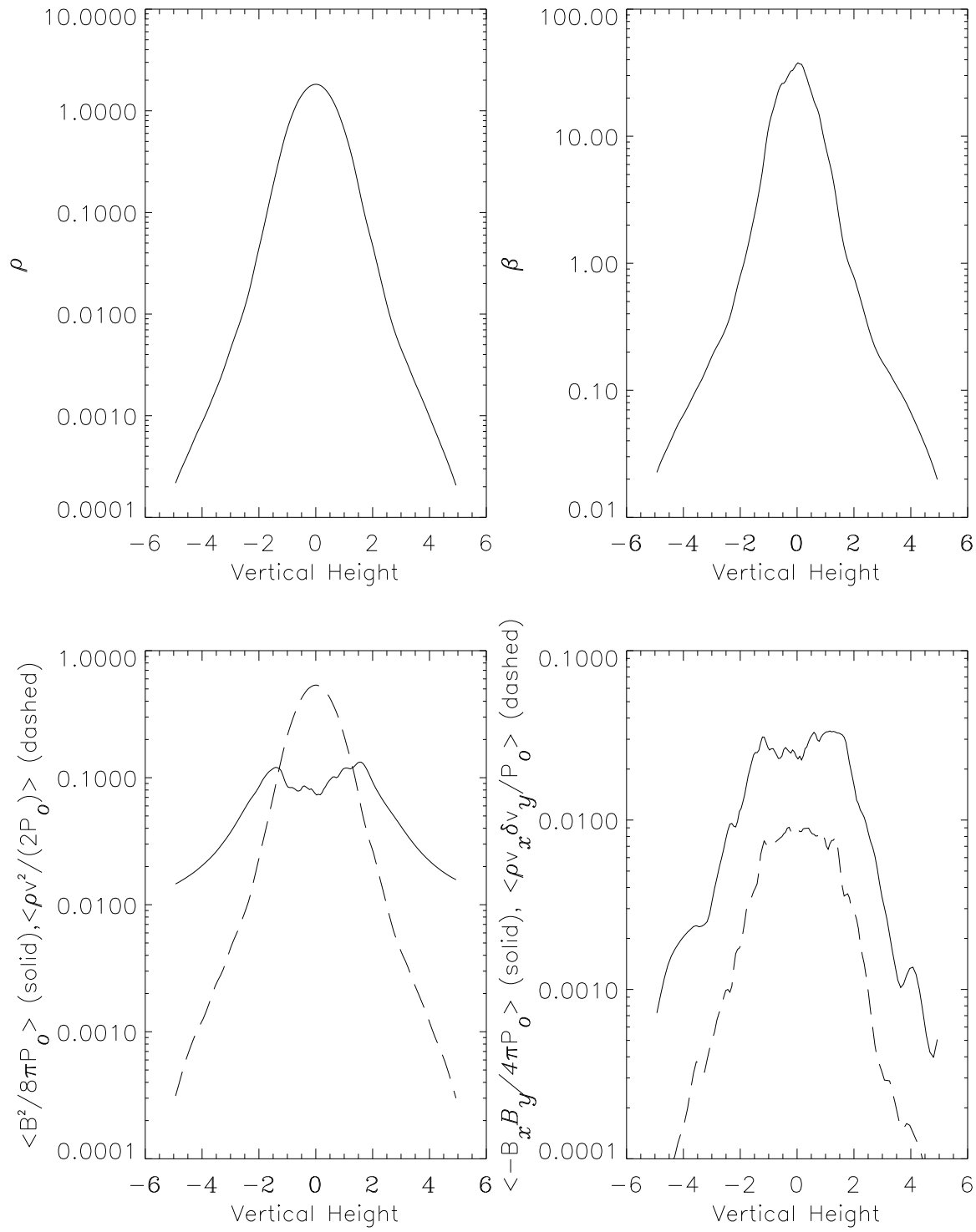
TABLE 3:
Volume and Time Averaged Quantities in Run ZN1

Quantity f	$\langle f \rangle^a$ ($\times 10^{-2}$)	$\langle \delta f^2 \rangle^{1/2a}$ ($\times 10^{-2}$)	min f ^a ($\times 10^{-2}$)	max f ^a ($\times 10^{-2}$)
$B_x^2/8\pi P_o$	0.11/0.054	0.059/0.036	0.0/0.0	0.23/0.19
$B_y^2/8\pi P_o$	2.23/1.23	1.06/0.67	0.0/0.0	3.89/1.96
$B_z^2/8\pi P_o$	0.060/0.052	0.081/0.036	0.01/0.006	0.49/0.18
$-B_x B_y/4\pi P_o$	0.54/0.15	0.24/0.10	-0.0004/-0.0001	0.95/0.45
$-B_x B_z/4\pi P_o$	-0.0034/0.0036	0.013/0.017	-0.059/-0.076	0.032/0.065
$-B_y B_z/4\pi P_o$	0.0072/-0.0049	0.022/0.011	-0.058/-0.054	0.071/0.045
$\rho v_x^2/2P_o$	0.79/0.05	0.39/0.039	0.0/0.0	2.2/0.22
$\rho \delta v_y^2/2P_o$	0.27/24.9	0.13/12.8	0.0/0.0	0.66/83.2
$\rho v_z^2/2P_o$	0.21/0.033	0.082/0.024	0.0/0.0	0.40/0.14
$\rho v_x \delta v_y/P_o$	0.25/0.022	0.21/0.021	-0.46/-0.07	1.26/0.14
ρ	76.8/0.53	0.14/0.14	76.5/0.29	77.1/0.81

^a The first number represents the average quantity f within $\pm 2H_z$; the second number represents the average quantity f for $|z| > 2H_z$. Averages were taken over 25 orbital times, after saturation.

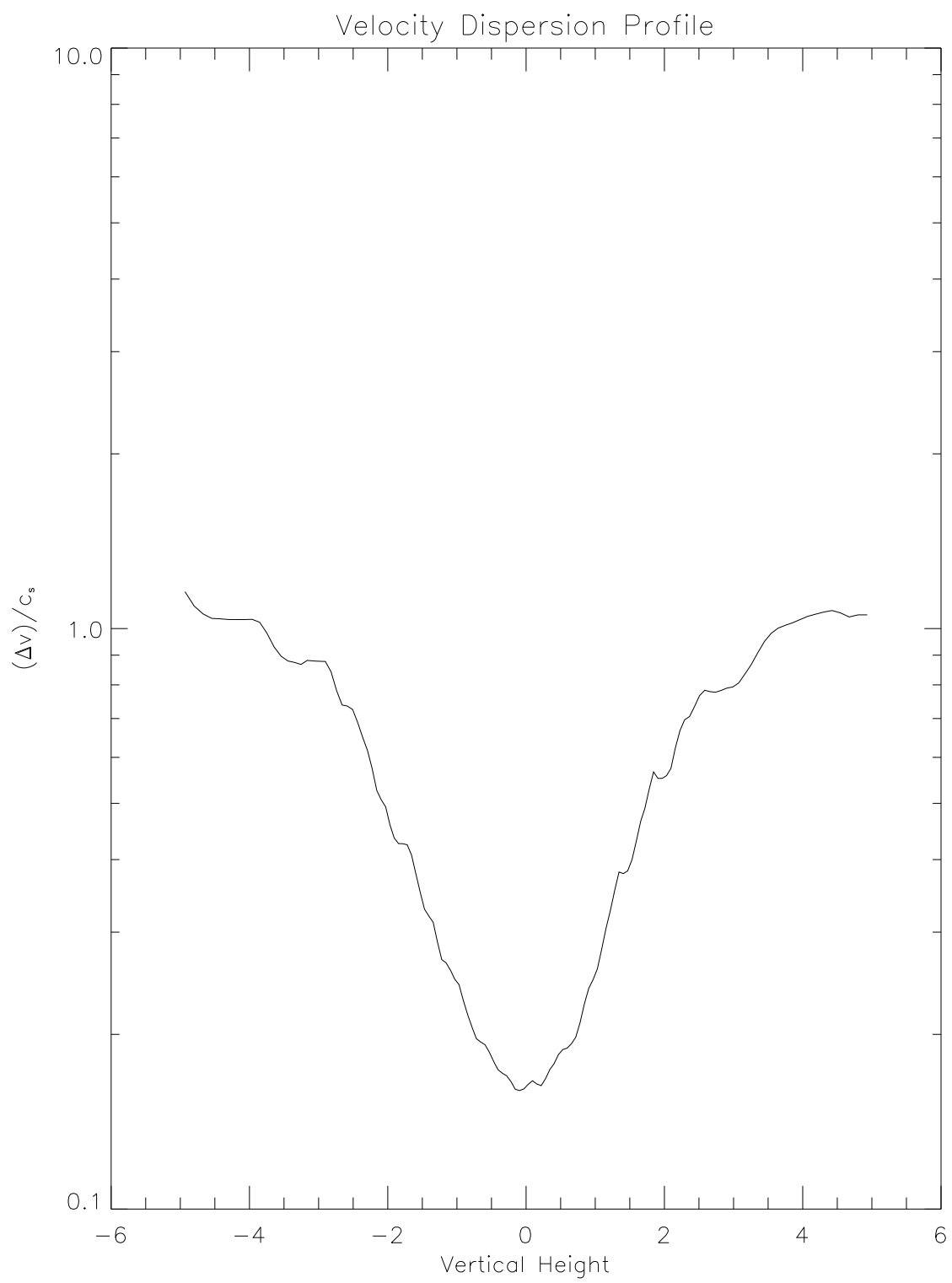
This figure "f1.jpg" is available in "jpg" format from:

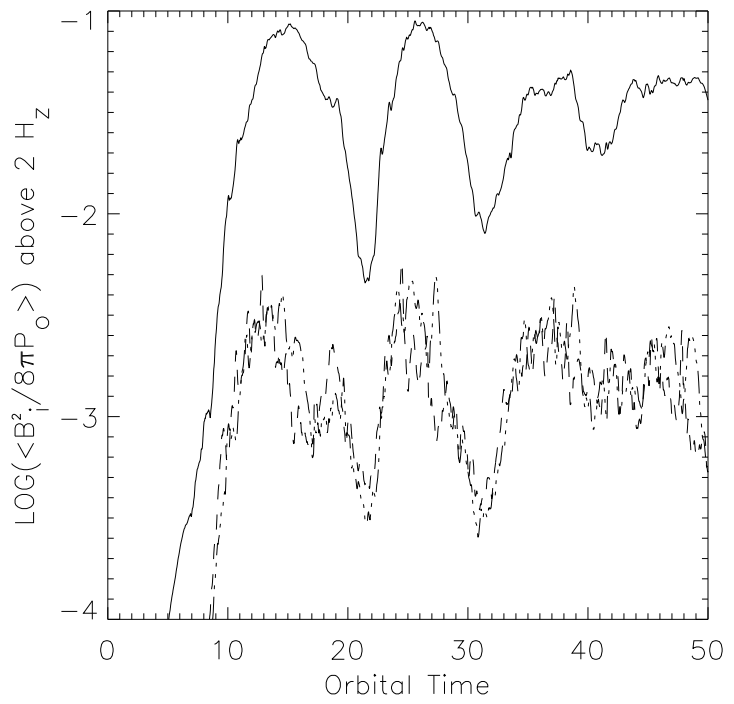
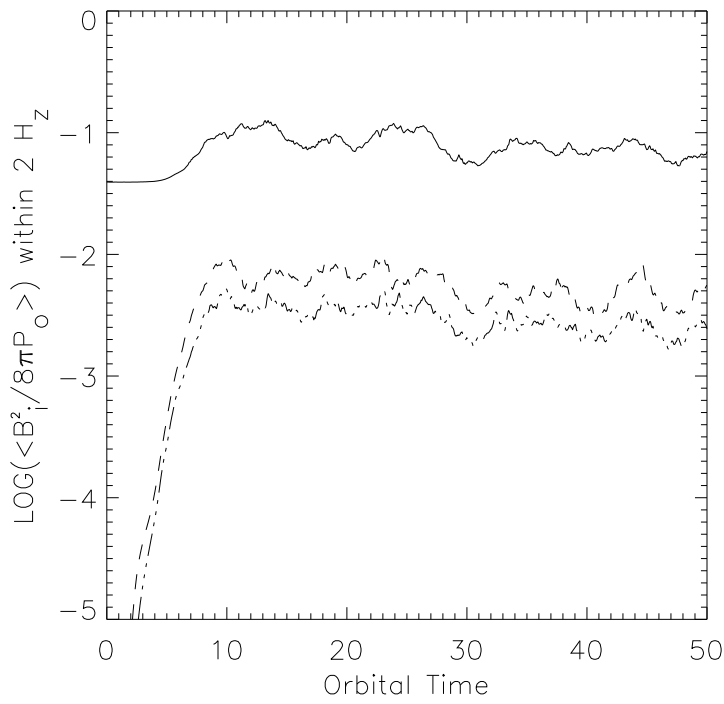
<http://arxiv.org/ps/astro-ph/9912135v1>

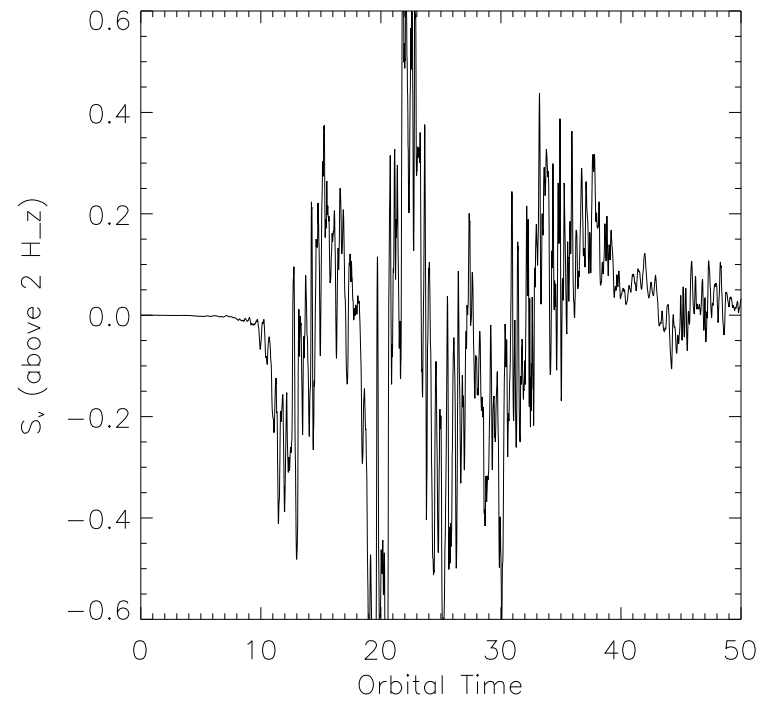
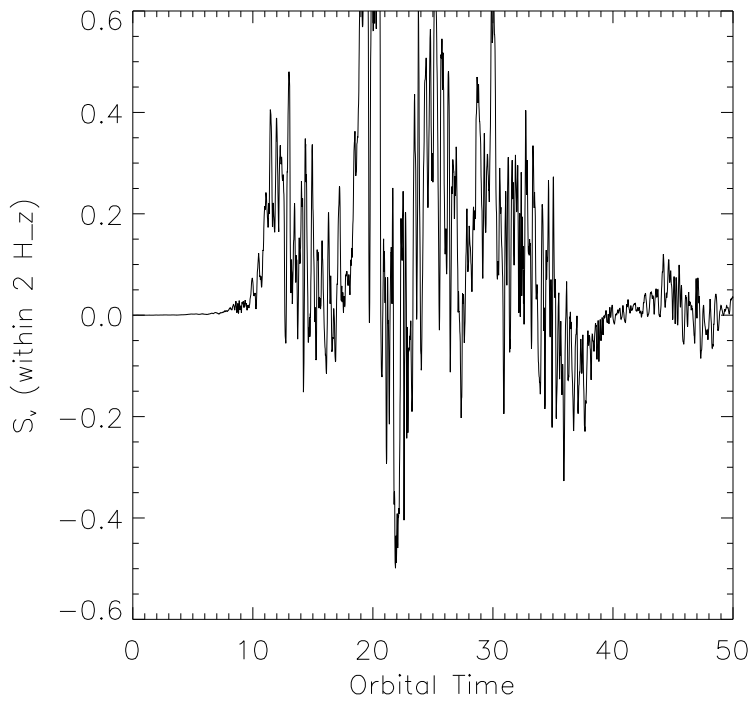


This figure "f3.jpg" is available in "jpg" format from:

<http://arxiv.org/ps/astro-ph/9912135v1>

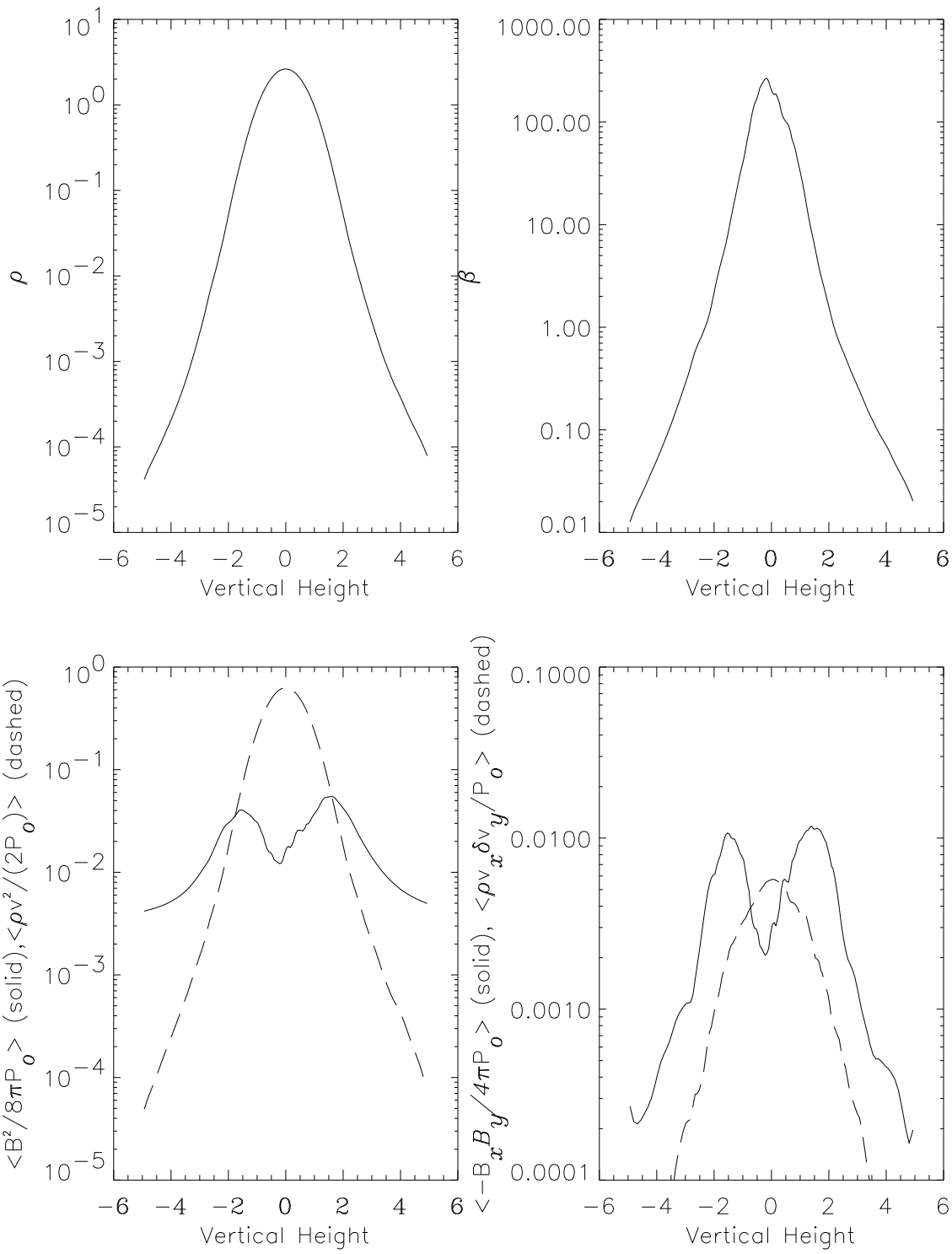


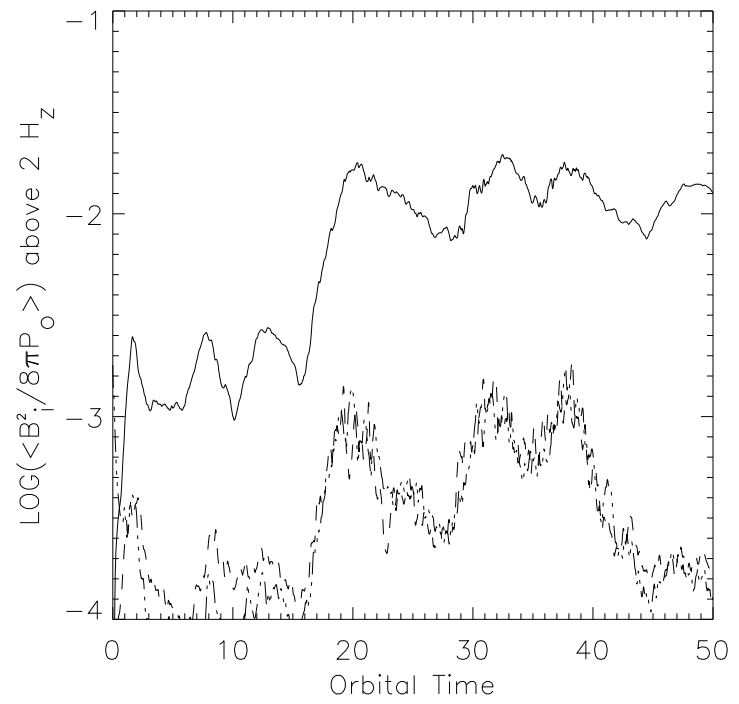
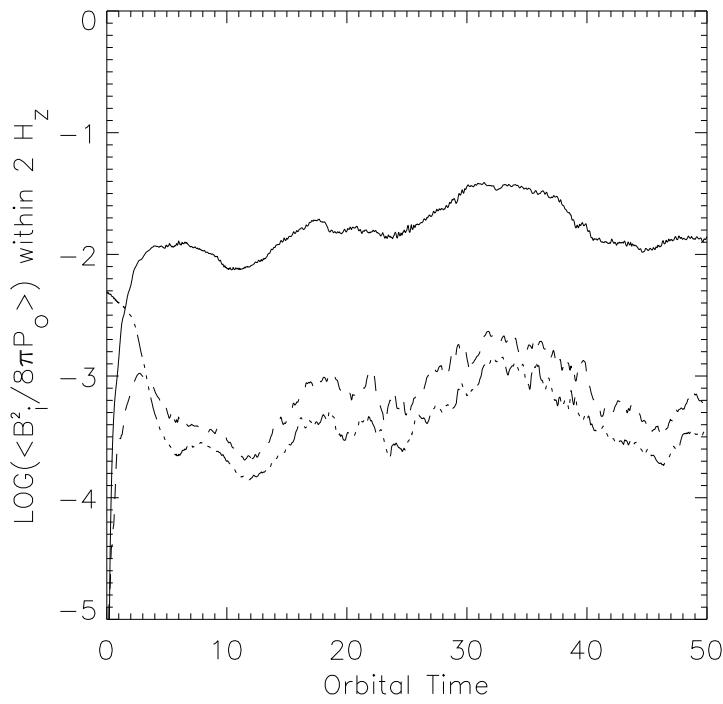




This figure "f7.jpg" is available in "jpg" format from:

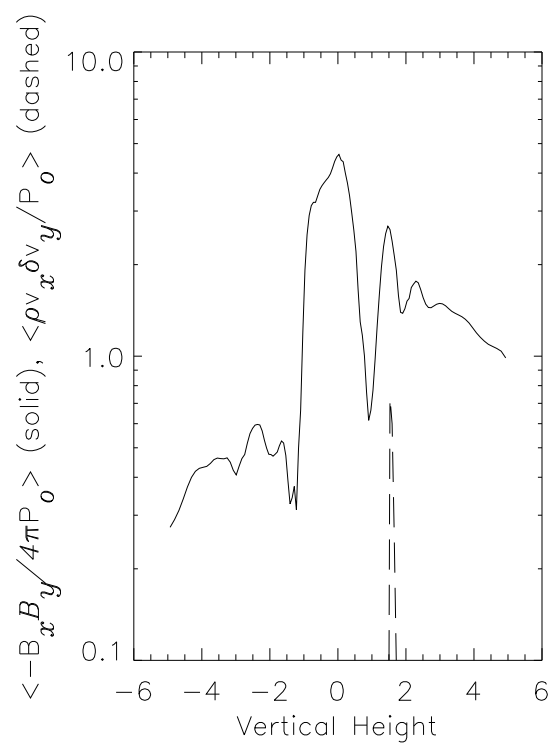
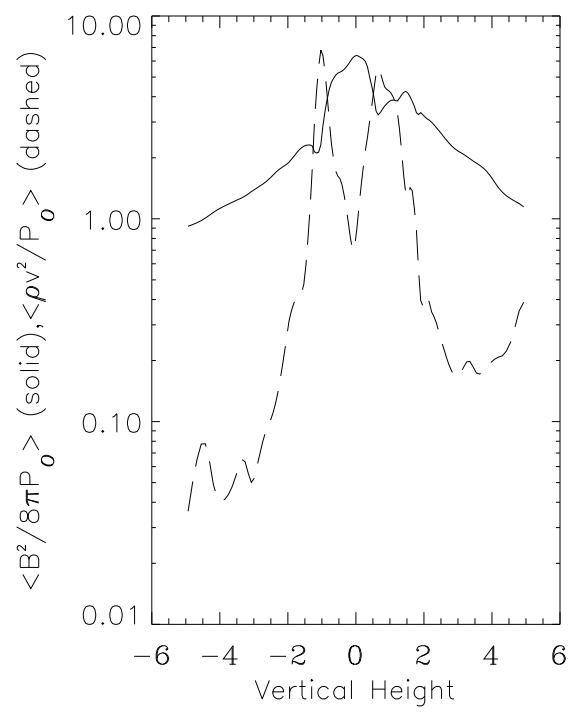
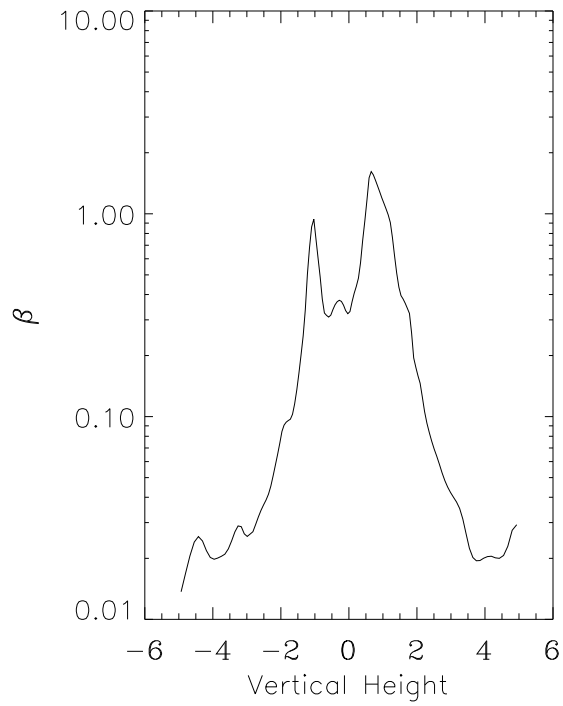
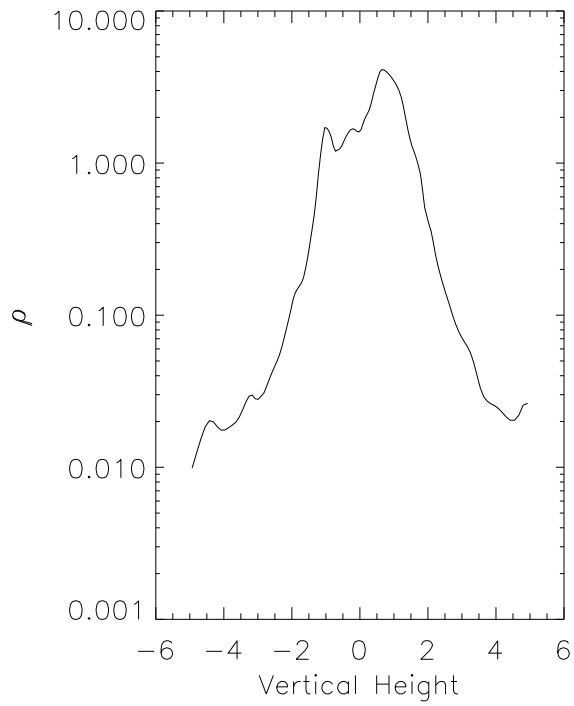
<http://arxiv.org/ps/astro-ph/9912135v1>





This figure "f10.jpg" is available in "jpg" format from:

<http://arxiv.org/ps/astro-ph/9912135v1>



Temperature Scale for a Disk Corona Surrounding a CTTS

